

Associated computational plasticity schemes for nonassociated frictional materials

K. Krabbenhoft^{1,2,*}, M. R. Karim¹, A. V. Lyamin¹ and S. W. Sloan¹

¹*Centre for Geotechnical Science and Engineering, University of Newcastle, Newcastle, NSW, Australia*

²*Department of Industrial and Civil Engineering, University of Southern Denmark, Odense, Denmark*

SUMMARY

A new methodology for computational plasticity of nonassociated frictional materials is presented. The new approach is inspired by the micromechanical origins of friction and results in a set of governing equations similar to those of standard associated plasticity. As such, procedures previously developed for associated plasticity are applicable with minor modification. This is illustrated by adaptation of the standard implicit scheme. Moreover, the governing equations can be cast in terms of a variational principle, which after discretization is solved by means of a newly developed second-order cone programming algorithm. The effects of nonassociativity are discussed with reference to localization of deformations and illustrated by means of a comprehensive set of examples. Copyright © 2012 John Wiley & Sons, Ltd.

Received 10 February 2011; Revised 10 October 2011; Accepted 11 October 2011

KEY WORDS: plasticity; nonassociated flow; friction; soil; mathematical programming

1. INTRODUCTION

The stress–strain behavior of geomaterials such as clay, sands, rock, and concrete can often, at least to a first approximation, be accounted for in terms of simple linear elastic/perfectly plastic models. Indeed, although a very large number of more complex models have been developed over the years, the simple linear elastic/perfectly plastic models remain widely used in engineering practice. Such models comprise three key ingredients: an elastic law, a yield criterion, and a flow rule. These components are all relatively straightforward to either measure or estimate. Regarding the flow rule, one often assumes a flow potential of the same functional form as the yield function, with a dilation coefficient replacing the friction coefficient of the yield function. The Mohr–Coulomb and Drucker–Prager models are often used as a basis for this approach. In this way, the excessive dilation predicted by the flow rule associated with the yield function may be adjusted to a more realistic magnitude.

Although the specification of an arbitrary flow rule in principle is straightforward, the deviation from associativity has a number of far reaching consequences. From a mathematical point of view, the introduction of a nonassociated flow rule usually leads to a situation where the governing equations, at some characteristic stress state, go from being elliptic to being hyperbolic. Physically, this loss of ellipticity indicates an instability where a homogeneous mode of deformation gives way to a localized deformation pattern defined by one or more shear bands [1–6]. Such localized modes of deformation give rise to a number of complications related to mesh dependence, internal length scales, and so on. Secondly, and more seriously, it has frequently been reported that numerical solutions to boundary value problems involving nonassociated constitutive models are much more

*Correspondence to: K. Krabbenhoft, Centre for Geotechnical Science and Engineering, University of Newcastle, Newcastle, NSW, Australia.

†E-mail: kristian.krabbenhoft@newcastle.edu.au

difficult to obtain than in the case where the flow rule is associated [7–10]. These complications have a tendency to be more pronounced for high (but realistic) values of the friction angle and the degree of nonassociativity. Similarly, for fixed material parameters, one usually observes a degradation of the performance as the number of finite elements in the model is increased.

These facts motivate a closer look at the physical origins of nonassociated flow rules and the numerical methods used to solve problems of frictional plasticity. In the following, inspired by the micromechanical origins of friction and its modeling in terms of plasticity theory, a new approach to computational plasticity for frictional (and generally nonassociated) materials is presented. The resulting scheme essentially approximates the original nonassociated problem as one of associated plasticity. Consequently, all the well-established numerical procedures for standard associated plasticity are applicable with little modification.

The paper is organized as follows. The governing equations are briefly summarized in Section 2 before the new approach of approximating general nonassociated plasticity models in terms of equivalent associated ones is presented in Section 3. In Section 4, two different solution algorithms are presented. The first one is a slight modification of the common fully implicit scheme by Simo and his coworkers [11, 12]. Secondly, following recent work of the authors [13–16], we formulate the governing equations in terms of a mathematical program. For certain yield criteria, notably Drucker–Prager, the resulting discrete programs may be solved very efficiently using a second-order cone programming solver, SONIC, recently developed by the authors. Next, in Section 5, the consequences of nonassociativity in terms of the ultimate load bearing capacity are discussed before the new numerical schemes are tested on some common boundary value problems in Section 6. These problems also highlight the consequences of nonassociated flow rules in terms of localization of deformations. Finally, conclusions are drawn in Section 7.

Matrix notation is used throughout with bold uppercase and lowercase letters representing matrices and vectors, respectively, and with T denoting the transpose.

2. GOVERNING EQUATIONS

In the following, the governing equations of rate-independent elastoplasticity are briefly summarized with emphasis on linear elastic/perfectly plastic models.

2.1. Equilibrium and strain–displacement equations

Assuming infinitesimal deformations, the strain–displacement relations are given by

$$\boldsymbol{\varepsilon} = \nabla \mathbf{u} \quad (1)$$

where $\mathbf{u} = (u_1, u_2, u_3)^T$ are the displacements, $\boldsymbol{\varepsilon} = (\varepsilon_{11}, \varepsilon_{22}, \varepsilon_{33}, 2\varepsilon_{12}, 2\varepsilon_{23}, 2\varepsilon_{31})^T$ are the strains, and ∇ is the usual linear strain–displacement operator.

The equilibrium equations and static boundary conditions are given by

$$\begin{aligned} \nabla^T \boldsymbol{\sigma} + \mathbf{b} &= \mathbf{0}, \quad \text{in } V \\ \mathbf{N}^T \boldsymbol{\sigma} &= \mathbf{t}, \quad \text{on } S \end{aligned} \quad (2)$$

where $\boldsymbol{\sigma} = (\sigma_{11}, \sigma_{22}, \sigma_{33}, \sigma_{12}, \sigma_{23}, \sigma_{31})^T$ are the stresses, V is the domain under consideration, S is its boundary, \mathbf{b} are body forces, \mathbf{t} are tractions, and $\mathbf{N} = \nabla(\mathbf{n}\mathbf{x}^T)$ with $\mathbf{n} = (n_1, n_2, n_3)^T$ being the outward normal to the boundary and $\mathbf{x} = (x_1, x_2, x_3)^T$ being the spatial coordinate.

2.2. Constitutive equations

Following classical plasticity theory, the stresses are limited by a yield function $F(\boldsymbol{\sigma}) \leq 0$. In the following, we will operate with the simple non-hardening Drucker–Prager yield function:

$$F(\boldsymbol{\sigma}) = q - Mp - k \quad (3)$$

where M is a friction coefficient and

$$\begin{aligned} p &= -\frac{1}{3}(\sigma_{11} + \sigma_{22} + \sigma_{33}) \\ q &= \left[\frac{1}{2}(\sigma_{11} - \sigma_{22})^2 + \frac{1}{2}(\sigma_{22} - \sigma_{33})^2 + \frac{1}{2}(\sigma_{33} - \sigma_{11})^2 + 3\sigma_{12}^2 + 3\sigma_{23}^2 + 3\sigma_{31}^2 \right]^{\frac{1}{2}} \end{aligned} \quad (4)$$

The Drucker–Prager parameters, M , N , and k , can be related to the more familiar Mohr–Coulomb parameters, ϕ , ψ , and c by matching the two criteria for plane strain conditions. Assuming associated flow, these relations are given by

$$M = \frac{3 \sin \phi}{\sqrt{3 + \sin^2 \phi}}, k = \frac{3c \cos \phi}{\sqrt{3 + \sin^2 \phi}} \quad (5)$$

where c and ϕ are the Mohr–Coulomb cohesion and friction angle, respectively. Analogously, a dilation angle, ψ , may be defined by

$$N = \frac{3 \sin \psi}{\sqrt{3 + \sin^2 \psi}} \quad (6)$$

The total strains are decomposed into elastic and plastic parts according to

$$\boldsymbol{\varepsilon} = \boldsymbol{\varepsilon}^e + \boldsymbol{\varepsilon}^p \quad (7)$$

where superscripts ‘e’ and ‘p’ refer to the elastic and plastic parts, respectively. In the following, the elastic strains are given by Hooke’s law as

$$\boldsymbol{\sigma} = \mathbb{D}^e \boldsymbol{\varepsilon}^e \iff \boldsymbol{\varepsilon}^e = \mathbb{C}^e \boldsymbol{\sigma} \quad (8)$$

where \mathbb{D}^e is the elastic stiffness modulus whereas $\mathbb{C}^e = (\mathbb{D}^e)^{-1}$ is the elastic compliance modulus.

The rate of plastic strain follows from a flow rule that in general is nonassociated and given by

$$\dot{\boldsymbol{\varepsilon}}^p = \dot{\lambda} \nabla G(\boldsymbol{\sigma}) \quad (9)$$

where G is a plastic potential, $\dot{\lambda} \geq 0$ is a plastic multiplier that satisfies $\dot{\lambda} F(\boldsymbol{\sigma}) = 0$, and $\nabla = (\partial/\partial\sigma_{11}, \dots, \partial/\partial\sigma_{31})^T$ is the gradient operator.

In the following, we use the plastic potential

$$G(\boldsymbol{\sigma}) = q - Np \quad (10)$$

where N is a dilation coefficient such that $N = M$ implies associated flow.

In summary, the constitutive model considered can be expressed in the following compact format:

$$\begin{aligned} \dot{\boldsymbol{\varepsilon}} &= \mathbb{C}^e \dot{\boldsymbol{\sigma}} + \dot{\lambda} \nabla G(\boldsymbol{\sigma}) \\ F(\boldsymbol{\sigma}) &\leq 0, \quad \dot{\lambda} F(\boldsymbol{\sigma}) = 0, \quad \dot{\lambda} \geq 0 \end{aligned} \quad (11)$$

where \mathbb{C}^e is the elastic compliance modulus and F and G are given by (3), (4), and (10).

3. FRICTION AND PLASTICITY

It is well known that the constitutive model (11) does not permit a variational formulation unless $G = F$, that is, unless the flow rule is associated [12, 15, 17]. In this case, the constitutive equations can be cast in terms of a variational statement similar to von Mises’s principle of maximum plastic dissipation. Moreover, if the yield function is convex, the governing equations may be cast in terms of a convex mathematical program. Such a formulation allows for a straightforward analysis of properties related to the existence and uniqueness of solutions. In the general nonassociated case, such a formulation is not possible. Although this shortcoming does not pose any fundamental obstacles to developing solution methods analogous to those of the associated case, the desirable mathematical properties of associated plasticity are lost. Moreover, whereas associated plasticity involves a symmetric tangent modulus, a nonassociated flow rule generally gives rise of an unsymmetric set of discrete finite element equations. Finally, although problems of associated plasticity

in many cases can be solved very efficiently using methods of modern mathematical programming [13, 14, 18], such formulations are not possible in the nonassociated case.

Motivated by the relative efficiency and robustness of numerical algorithms for associated plasticity, a new numerical formulation that retains the desirable properties of associated computational plasticity, but which is applicable to general nonassociated models, is presented in the following. It should be noted, however, that the characteristics of nonassociated plasticity in terms of localization of deformations are retained. This includes the apparent global softening often observed in boundary value problems involving a perfectly plastic nonassociated model. Similarly, the non-uniqueness of solutions implied by most nonassociated models also persists and is manifested by a strong sensitivity to the finite element mesh, boundary conditions, and so on. These points are illustrated and discussed in more detail in Section 6.

3.1. Micromechanics of friction

The basic idea behind the new formulation derives from the structure of the internal dissipation associated with constitutive models of the type (11). In p - q space, the plastic strain rates are given by

$$\dot{\varepsilon}_v^p = \dot{\lambda} \frac{\partial G}{\partial p} = -\dot{\lambda} N; \dot{\varepsilon}_s^p = \dot{\lambda} \frac{\partial G}{\partial q} = \dot{\lambda} \quad (12)$$

where ε_v^p and ε_s^p are the volumetric and deviatoric strains conjugate to p and q , respectively. The internal dissipation associated with the model (11) is then given by

$$\begin{aligned} D &= p\dot{\varepsilon}_v^p + q\dot{\varepsilon}_s^p \\ &= (-Np + q)\dot{\lambda} \\ &= [k + (M - N)p]\dot{\lambda} \\ &= [k + (M - N)p]\dot{\varepsilon}_s^p \end{aligned} \quad (13)$$

This expression for the internal dissipation reveals several interesting, albeit well-known, features. Firstly, for an associated material ($N = M$), the dissipation is proportional to the internal cohesion, k . As such, no internal dissipation takes place for a purely frictional material ($k = 0$), which is in obvious contrast to experimental evidence. Secondly, for $N < M$, the dissipation is proportional to an apparent cohesion, which comprises two terms: the internal cohesion k and a contribution $(M - N)p$, which stems from the prescribed degree of nonassociativity. The interpretation of the latter term as an apparent cohesion is consistent with the viewpoint that friction results from the mechanical interaction of microscopic asperities on the surfaces of the solids in contact [19]. With the stresses at the scale of the asperities being much greater than the elastic limit of the material, it is primarily plastic deformations at the microscale that govern the macroscopically observed frictional resistance. This point is illustrated in Figure 1, which shows two rough surfaces under different levels of confining pressure. The plastic shearing may be assumed to be of the ductile, purely cohesive kind. For brittle materials such as sand grains, this assumption is justified by the very high stress level at the scale of the asperities, which effectively renders the otherwise brittle material ductile. The apparent shear strength of each assembly thus derives exclusively from the geometric changes induced by the confining pressure and with Coulomb friction implying a linear relation between apparent shear strength and confining pressure. This interpretation motivates rewriting the yield function (3) as

$$F = q - Np - k^*(p) \quad (14)$$

where

$$k^*(p) = k + (M - N)p \quad (15)$$

is the apparent, pressure-dependent, cohesion. This material parameter embodies all the complexities of the actual micromechanics of the frictional interfaces and their evolution in response to the

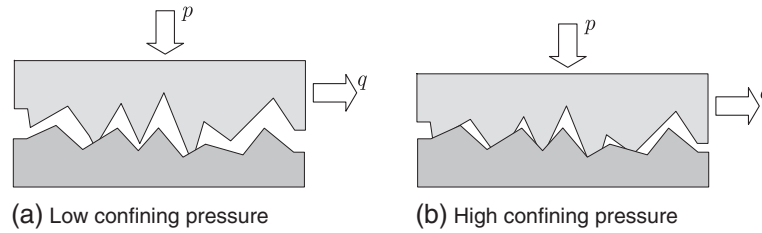


Figure 1. Microscopic origins of friction as plastic shearing of asperities. A higher confining pressure implies a higher degree of interlocking of the asperities and thereby a higher apparent shear strength. (a) Low confining pressure. (b) High confining pressure.

applied loads. As such, its relative simplicity is surprising, but nevertheless found to be appropriate for a very broad range of materials, although there are also a number of noteworthy exceptions as discussed for example in [19].

3.2. Time-discrete formulation

Suppose now that the apparent cohesion, k^* , is known. The associated flow rule then produces the desired result, namely the plastic strain rates (12). In the solution of boundary value problems, the apparent cohesion is of course not known a priori as it is directly proportional to the pressure that is to be determined as part of the solution. However, assuming that such problems are solved incrementally via a sequence of pseudo-time steps, some parts of the yield function may, in principle, be evaluated implicitly whereas other parts may be evaluated explicitly. Assume that the state at time t_n is known. The yield condition imposed at t_{n+1} may then be approximated as

$$F_{n+1} \approx F_{n+1}^* = q_{n+1} - Np_{n+1} - k_n^* \quad (16)$$

where

$$k_n^* = k^*(p_n) = k + (M - N)p_n \quad (17)$$

Again, the associated flow rule produces the desired time-discrete result, namely

$$\begin{aligned} (\Delta \varepsilon_v^p)_{n+1} &= \Delta \lambda_{n+1} \left. \frac{\partial F^*}{\partial p} \right|_{n+1} = -\Delta \lambda_{n+1} N \\ (\Delta \varepsilon_s^p)_{n+1} &= \Delta \lambda_{n+1} \left. \frac{\partial F^*}{\partial q} \right|_{n+1} = \Delta \lambda_{n+1} \end{aligned} \quad (18)$$

However, the explicit evaluation of the apparent cohesion means that the original yield function may be exceeded for the new stress state at t_{n+1} . Similarly, the approximation may imply plastic yielding for stress states that would otherwise be deemed purely elastic (see Figure 2). However, for small enough increments, that is, for $t_{n+1} - t_n \rightarrow 0$, it would be expected that the error introduced by the explicit evaluation of the apparent cohesion would tend to vanish. Numerical experiments confirm this supposition as will be discussed in more detail in Section 6.

4. SOLUTION ALGORITHMS

In the following, three different algorithms are presented. Firstly, the standard implicit scheme by Simo and Taylor [11] is summarized. Secondly, this scheme is used as a basis for solution via the apparent cohesion interpretation outlined above. Finally, the governing equations are cast in terms of a variational principle, which is subsequently discretized to arrive at a mathematical programming formulation.

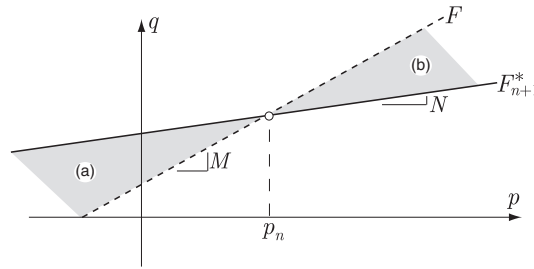


Figure 2. Explicit evaluation of apparent cohesion: original and approximate yield functions. The area indicated by (a) is non-permissible according to the original yield function but permissible according to the approximate yield function. Similarly, the area indicated by (b) is non-permissible according to the approximate yield function but is within the elastic domain according to the original yield function.

Table I. Standard implicit scheme.

| |
|---|
| <p>Time steps: $n = 0, \dots, n_{\max}$</p> <p>$\mathbf{u}_{n+1}^0 = \mathbf{u}_n, \quad \boldsymbol{\sigma}_{n+1}^0 = \boldsymbol{\sigma}_n, \quad \Delta\lambda_{n+1}^0 = 0$</p> <p>Iterations: $j = 0, \dots$, until convergence</p> <p>$\mathbf{r}_{n+1}^j = \mathbf{p}_{\text{ext}} - \int_V \mathbf{B}^T \boldsymbol{\sigma}_{n+1}^j \, dV; \quad (\mathbf{K}_t)_{n+1}^j = \int_V \mathbf{B}^T (\mathbb{D}_c^{\text{ep}})_{n+1}^j \mathbf{B} \, dV$</p> <p>$\delta \mathbf{u} = [(\mathbf{K}_t)_{n+1}^j]^{-1} \mathbf{r}_{n+1}^j$</p> <p>$\mathbf{u}_{n+1}^{j+1} = \mathbf{u}_{n+1}^j + \delta \mathbf{u}$</p> <p>$\Delta \boldsymbol{\varepsilon}_{n+1}^{j+1} = \mathbf{B}(\mathbf{u}_{n+1}^{j+1} - \mathbf{u}_n)$</p> <p>$(\boldsymbol{\sigma}_{n+1}^{j+1}, \Delta\lambda_{n+1}^{j+1}) = SI(\boldsymbol{\sigma}_n, \Delta \boldsymbol{\varepsilon}_{n+1}^{j+1})$</p> <p>end iterations</p> <p>end time step</p> |
|---|

4.1. Standard implicit scheme

Using standard finite element terminology, the standard implicit scheme proceeds from a known state at time t_n by first computing a displacement increment according to

$$\mathbf{K}_t \delta \mathbf{u} = \mathbf{r} \tag{19}$$

where \mathbf{K}_t is the tangent stiffness matrix obtained by consistent linearization of the time-discrete governing equations and \mathbf{r} is the total out-of-balance force. On the basis of this displacement increment, a strain increment is computed as the difference between the current displacement and the displacement at the beginning of the time step. Next, the corresponding stress state is determined by means of the closest-point projection scheme. This will usually result in a change in the out-of-balance force, and the process is repeated until convergence, that is, until the out-of-balance forces vanishes to within some acceptable tolerance. The full scheme is summarized in Table I. The stress integration is here represented by $SI()$ whereas \mathbb{D}_c^{ep} is the consistent elastoplastic tangent modulus. The external load vector is given by \mathbf{p}_{ext} .

Concerning the detection of plasticity in a given time step, it is common practice to first compute a so-called elastic trial stress state given by

$$\boldsymbol{\sigma}_{\text{tr}} = \boldsymbol{\sigma}_n + \mathbb{D}^e \Delta \boldsymbol{\varepsilon}_{n+1}^{j+1} \tag{20}$$

If this trial stress state is within the yield surface, the new stress state $\boldsymbol{\sigma}_{n+1}^{j+1}$ is set equal to $\boldsymbol{\sigma}_{\text{tr}}$ and the stress integration is complete. If, on the other hand, the trial stress lies outside the yield surface, a full elastoplastic stress integration is performed.

4.1.1. Stress integration. The material point stress integration of the fully implicit scheme is well documented in the literature [12, 17] and will here only be briefly summarized. For the Drucker–Prager model considered in this paper, the notable feature is that the stress integration can be carried out in closed form. In performing the integration, a distinction must be made between stress states that imply a return to the regular part of the yield surface and stress states that imply a return to the apex.

(I) *Return to regular part of the Drucker–Prager cone.* Assuming that the new state is plastic and lies on the regular part of the yield surface, the local governing equations are given by

$$\begin{aligned}\Delta \boldsymbol{\varepsilon}_{n+1} &= \mathbb{C}^e (\boldsymbol{\sigma}_{n+1} - \boldsymbol{\sigma}_n) + \Delta \lambda_{n+1} \nabla G(\boldsymbol{\sigma}_{n+1}) \\ F(\boldsymbol{\sigma}_{n+1}) &= 0\end{aligned}\quad (21)$$

Introducing the trial stress state

$$\boldsymbol{\sigma}_{\text{tr}} = \boldsymbol{\sigma}_n + \mathbb{D}^e \Delta \boldsymbol{\varepsilon}_{n+1} \quad (22)$$

the local equations may be written as

$$\begin{aligned}\boldsymbol{\sigma}_{n+1} - \boldsymbol{\sigma}_{\text{tr}} + \Delta \lambda_{n+1} \mathbb{D}^e \nabla G(\boldsymbol{\sigma}_{n+1}) &= \mathbf{0} \\ F(\boldsymbol{\sigma}_{n+1}) &= 0\end{aligned}\quad (23)$$

For the Drucker–Prager criterion, and assuming isotropic elasticity and non-hardening plasticity, it can be shown [17] that the gradients of F and G at the new state and at the trial state are identical. This property can be used to show that the solution to the above equations is given by

$$\begin{aligned}\Delta \lambda_{n+1} &= [\nabla F(\boldsymbol{\sigma}_{\text{tr}})^\top \mathbb{D}^e \nabla G(\boldsymbol{\sigma}_{\text{tr}})]^{-1} F(\boldsymbol{\sigma}_{\text{tr}}) \\ \boldsymbol{\sigma}_{n+1} &= \boldsymbol{\sigma}_{\text{tr}} - \Delta \lambda_{n+1} \mathbb{D}^e \nabla G(\boldsymbol{\sigma}_{\text{tr}})\end{aligned}\quad (24)$$

These solutions constitute the first iterates in a standard Newton scheme applied to (23) from an initial point given by $(\boldsymbol{\sigma}_{n+1}^0, \Delta \lambda_{n+1}^0) = (\boldsymbol{\sigma}_{\text{tr}}, 0)$.

The consistent tangent modulus is given by

$$\mathbb{D}_c^{\text{ep}} = \mathbb{D}_c^e - \frac{\mathbb{D}_c^e \nabla G(\boldsymbol{\sigma}_{\text{tr}}) \nabla F(\boldsymbol{\sigma}_{\text{tr}})^\top \mathbb{D}_c^e}{\nabla F(\boldsymbol{\sigma}_{\text{tr}})^\top \mathbb{D}_c^e \nabla G(\boldsymbol{\sigma}_{\text{tr}})} \quad (25)$$

where

$$\mathbb{D}_c^e = [\mathbb{C}^e + \Delta \lambda_{n+1} \nabla^2 G(\boldsymbol{\sigma}_{n+1})]^{-1} \quad (26)$$

Note that this quantity must be evaluated for $\boldsymbol{\sigma}_{n+1}$ rather than $\boldsymbol{\sigma}_{\text{tr}}$.

(II) *Return to apex.* In the case where the trial stress state is returned to the apex, the new stress state is given by [17, 20, 21]

$$\boldsymbol{\sigma}_{n+1} = 3 \frac{k}{M} \mathbf{a} \quad (27)$$

where

$$\mathbf{a} = \frac{1}{3}(1, 1, 1, 0, 0, 0)^\top \quad (28)$$

The consistent tangent modulus is given by

$$\mathbb{D}_c^{\text{ep}} = \mathbf{0} \quad (29)$$

reflecting the singularity of the apex [17, 20, 21].

Choice of return path. The integration of the local equations proceeds by first determining the stress point (24). This point may be located on the actual yield surface or on the surface $F' = Mp - q - \hat{k} = 0$. The latter case indicates that a return to the apex in accordance with (27) should have been performed. In practice, this return is subsequently chosen if $M \mathbf{a}^\top \boldsymbol{\sigma}_{n+1} > k$ where $\boldsymbol{\sigma}_{n+1}$ is given by (24).

4.2. Implicit scheme–apparent cohesion approach

The adaptation of the standard implicit scheme to the apparent cohesion approach discussed in Section 3 is relatively straightforward. Essentially, the only difference is that we now operate with a yield function F_{n+1}^* as given by (16). This yield function, which also plays the role of plastic potential, is updated at the beginning of each time step, and all subsequent operations are then identical to those of the standard implicit scheme with an associated flow rule. Using this approach, it should be noted that stress states violating the original yield function are possible. Likewise, stress states that according to the original yield condition would be considered elastic will in some cases be recorded as being plastic. An example is shown in Figure 3. The time stepping is here initiated [Figure 3(a)] from a point (p_n, q_n) that according to both yield conditions is elastic. The new state (p_{n+1}, q_{n+1}) is also elastic according to the approximate yield function F_{n+1}^* but violates the original yield function F . In the subsequent step [Figure 3(b)], a new approximate yield function F_{n+2}^* is constructed, and the stress state at the end of the step, (p_{n+2}, q_{n+2}) , satisfies $F_{n+2}^* = 0$ while it would be considered elastic according to the original yield function F . As already mentioned, these errors have a tendency to vanish as the step size is reduced.

To further limit the drift from the original yield surface, it is useful to introduce a tension cut-off that coincides with the apex of the original yield surface. For the Drucker–Prager criterion, we use

$$T = -p - k_t \tag{30}$$

where T coincides with the apex of F for $k_t = k/M$ (see Figure 4).

4.2.1. Stress integration. The stress integration follows that of the standard implicit scheme derived above except that more than one yield surface may be active. In this case, it is useful to consider the integration as the solution to the closest-point projection problem [12, 22]:

$$\begin{aligned} &\text{minimize}_{\sigma_{n+1}} && -\frac{1}{2}(\sigma_{n+1} - \sigma_{tr})^T C^e (\sigma_{n+1} - \sigma_{tr}) \\ &\text{subject to} && F^*(\sigma_{n+1}) \leq 0 \\ & && T(\sigma_{n+1}) \leq 0 \end{aligned} \tag{31}$$

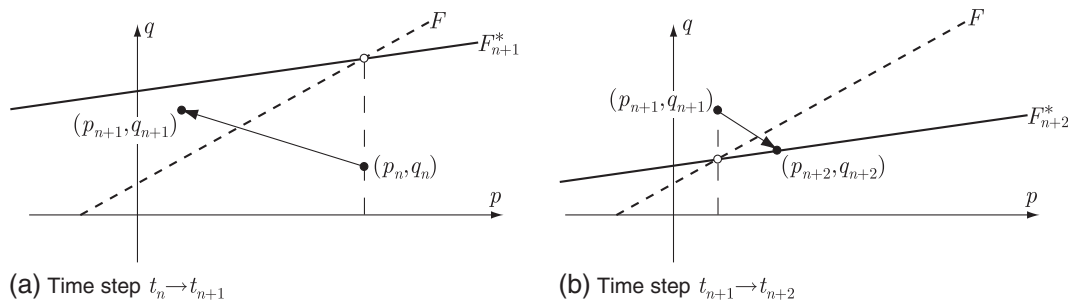


Figure 3. Two subsequent time steps using the apparent cohesion interpretation. (a) Time step $t_n \rightarrow t_{n+1}$. (b) Time step $t_{n+1} \rightarrow t_{n+2}$.

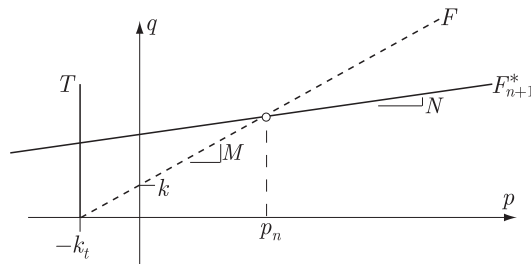


Figure 4. Original and approximate yield surfaces augmented by a tension cut-off.

This problem (which implies Koiter's rule [22, 23]) can again be solved in closed form by considering four different types of solutions: (i) return to the regular part of the Drucker–Prager cone, (ii) return to the tension cut-off plane, (iii) return to the intersection between the tension cut-off and the Drucker–Prager cone, and (iv) return to the apex. We note that the last possibility in practice is redundant as the tension cut-off usually will be such that the apex of F_{n+1}^* is not contained within the elastic domain. Each of these four different types of return comes with a different consistent tangent modulus as detailed in the following.

- (I) *Return to regular part of the Drucker–Prager cone.* Assuming that the new state is plastic and lies on the regular part of the yield surface, we have

$$\begin{aligned}\Delta\lambda_{n+1} &= [\nabla F_{n+1}^*(\boldsymbol{\sigma}_{tr})^\top \mathbb{D}^e \nabla F_{n+1}^*(\boldsymbol{\sigma}_{tr})]^{-1} F_{n+1}^*(\boldsymbol{\sigma}_{tr}) \\ \boldsymbol{\sigma}_{n+1} &= \boldsymbol{\sigma}_{tr} - \Delta\lambda_{n+1} \mathbb{D}^e \nabla F_{n+1}^*(\boldsymbol{\sigma}_{tr})\end{aligned}\quad (32)$$

The consistent tangent modulus is given by (25) with $F = G = F_{n+1}^*$.

- (II) *Return to apex.* In the case where the trial stress state is returned to the apex, the new stress state is given by

$$\boldsymbol{\sigma}_{n+1} = 3 \frac{k_n^*}{N} \mathbf{a} \quad (33)$$

where \mathbf{a} is given by (28). As in the standard case, we have $\mathbb{D}_c^{\text{ep}} = \mathbf{0}$.

- (III) *Return to tension cut-off.* In this case, the new state is given by

$$\begin{aligned}\Delta\lambda_{n+1} &= (\mathbf{a}^\top \mathbb{D}^e \mathbf{a})^{-1} (\mathbf{a}^\top \boldsymbol{\sigma}_{tr} - k_t) \\ \boldsymbol{\sigma}_{n+1} &= \boldsymbol{\sigma}_{tr} - \Delta\lambda_{n+1} \mathbb{D}^e \mathbf{a}\end{aligned}\quad (34)$$

whereas the consistent tangent modulus is given by

$$\mathbb{D}_c^{\text{ep}} = \mathbb{D}^e - \mathbb{D}^e \mathbf{a} (\mathbf{a}^\top \mathbb{D}^e \mathbf{a})^{-1} \mathbf{a}^\top \mathbb{D}^e \quad (35)$$

Note that this is identical to the ‘continuum’ tangent modulus, that is, the tangent modulus corresponding to infinitesimal time steps, as $\nabla^2 T = \mathbf{0}$.

- (IV) *Return to intersection between Drucker–Prager cone and tension cut-off.* In the case where the stress state is returned to the intersection between the Drucker–Prager cone and the tension cut-off, the return mapping operations may be split into a pure deviatoric part followed by a purely hydrostatic part. The deviatoric part follows that of a regular cone return with a yield function given by

$$F_q^* = q - (k^* - Nk_t) \quad (36)$$

This surface passes through the cone/cut-off intersection at constant $q = k - Mk_t$. The return mapping equations are given by

$$\begin{aligned}\Delta\lambda_{q,n+1} &= [\nabla F_{q,n+1}^*(\boldsymbol{\sigma}_{tr})^\top \mathbb{D}^e \nabla F_{q,n+1}^*(\boldsymbol{\sigma}_{tr})]^{-1} F_{q,n+1}^*(\boldsymbol{\sigma}_{tr}) \\ \boldsymbol{\sigma}_{q,n+1} &= \boldsymbol{\sigma}_{tr} - \Delta\lambda_{q,n+1} \mathbb{D}^e \nabla F_{q,n+1}^*(\boldsymbol{\sigma}_{tr})\end{aligned}\quad (37)$$

With q thus fixed, a tension cut-off return is performed according to

$$\begin{aligned}\Delta\lambda_{p,n+1} &= (\mathbf{a}^\top \mathbb{D}^e \mathbf{a})^{-1} (\mathbf{a}^\top \boldsymbol{\sigma}_{q,n+1} - k_t) \\ \boldsymbol{\sigma}_{n+1} &= \boldsymbol{\sigma}_{q,n+1} - \Delta\lambda_{p,n+1} \mathbb{D}^e \mathbf{a}\end{aligned}\quad (38)$$

Finally, the consistent tangent modulus is given by

$$\mathbb{D}_c^{\text{ep}} = \mathbb{D}_c^e - \mathbb{D}_c^e \nabla F (\nabla F^\top \mathbb{D}_c^e \nabla F)^{-1} \nabla F^\top \mathbb{D}_c^e \quad (39)$$

where

$$\mathbb{D}^e = [\mathbb{C}^e + \Delta\lambda_{q,n+1} \nabla^2 F_{n+1}^*(\boldsymbol{\sigma}_{n+1})]^{-1} \quad (40)$$

and

$$\nabla \mathbf{F} = [\nabla F_{n+1}^*(\boldsymbol{\sigma}_{n+1}), \mathbf{a}] \quad (41)$$

Choice of return path. The integration of the local equations proceeds by first assuming a regular cone return. If the resulting stress state violates the corresponding yield condition, an apex return is attempted. This return is deemed valid if the tension cut-off criterion is satisfied. If not, a regular tension cut-off return is attempted, and if the resulting stress state satisfies both yield conditions, it is taken as being the correct stress. If not, the combined cone/tension cut-off return is the only possibility of satisfying the local constitutive relations.

4.2.2. *Line search.* For time steps above a certain magnitude, the global iterations may fail to converge. In such cases, the iterative scheme may be supplemented with a line search. The idea here is to introduce a damping factor such that the displacements (see Table I) are updated as

$$\mathbf{u}_{n+1}^{j+1} = \mathbf{u}_{n+1}^j + \alpha \delta \mathbf{u}, \quad 0 < \alpha \leq 1 \quad (42)$$

where α is the damping factor. This is chosen so as to minimize the norm of the residual, that is,

$$\underset{\alpha}{\text{minimize}} \quad \|\mathbf{r}(\mathbf{u}_{n+1}^j + \alpha \delta \mathbf{u})\| \quad (43)$$

An approximate optimality condition to this minimization problem is given by

$$\delta \mathbf{u}^T \mathbf{r}(\mathbf{u}_{n+1}^j + \alpha \delta \mathbf{u}) = 0 \quad (44)$$

Finally, an approximate value of α is found by interpolating $\delta \mathbf{u}^T \mathbf{r}(\mathbf{u}_{n+1}^j + \alpha \delta \mathbf{u})$ linearly between $\alpha = 0$ and $\alpha = 1$. The resulting approximation to the above equation is then solved for α to yield

$$\alpha = \min \left\{ 1, \frac{\delta \mathbf{u}^T \mathbf{r}(\mathbf{u}_{n+1}^j)}{\delta \mathbf{u}^T [\mathbf{r}(\mathbf{u}_{n+1}^j) - \mathbf{r}(\mathbf{u}_{n+1}^j + \delta \mathbf{u})]} \right\} \quad (45)$$

Although more elaborate schemes are possible (see, e.g., [24]), the performance of the simple one described above has shown to be satisfactory over a large range of typical boundary value problems.

4.3. Mathematical programming formulation

An interesting possibility of the new apparent cohesion interpretation of nonassociated elastoplasticity is the application of mathematical programming methods. Although such methods now are well developed for limit analysis [18, 25–27] and further have been applied to problems of step-by-step elastoplasticity [13, 14], a serious limitation is that the flow rule must be associated. However, the new formulation presented in this paper paves the way for extending the methods previously developed for limit analysis to general nonassociated elastoplasticity. This includes solution algorithms such as the ones cited above, specialized finite element formulations [13, 22, 28], and mesh adaptivity schemes [29, 30].

A suitable starting point for the development of a mathematical programming algorithm for elastoplasticity is the following time-discrete variational principle [13]:

$$\begin{aligned} \min_{\mathbf{u}_{n+1}} \max_{\boldsymbol{\sigma}_{n+1}} & \quad - \int_V (\boldsymbol{\sigma}_{n+1} - \boldsymbol{\sigma}_n)^T \mathbb{C}^e (\boldsymbol{\sigma}_{n+1} - \boldsymbol{\sigma}_n) dV + \int_V \boldsymbol{\sigma}_{n+1}^T [\boldsymbol{\varepsilon}(\mathbf{u}_{n+1}) - \boldsymbol{\varepsilon}(\mathbf{u}_n)] dV \\ & \quad - \int_V \mathbf{b}^T (\mathbf{u}_{n+1} - \mathbf{u}_n) dV - \int_S \mathbf{t}^T (\mathbf{u}_{n+1} - \mathbf{u}_n) dV \\ \text{subject to} & \quad F(\boldsymbol{\sigma}_{n+1}) \leq 0 \end{aligned} \quad (46)$$

Assuming small deformations, that is, $\boldsymbol{\varepsilon}(\mathbf{u}) = \nabla \mathbf{u}$, and using standard methods of variational calculus [12, 13, 31], it may be shown that the optimality conditions associated with this min–max problem are given by

$$\begin{aligned} \nabla^\top \boldsymbol{\sigma}_{n+1} + \mathbf{b} &= \mathbf{0}, \text{ in } V \\ N^\top \boldsymbol{\sigma}_{n+1} &= \mathbf{t}, \text{ on } S \\ \nabla \mathbf{u}_{n+1} - \nabla \mathbf{u}_n &= \mathbb{C}(\boldsymbol{\sigma}_{n+1} - \boldsymbol{\sigma}_n) + \Delta \lambda_{n+1} \nabla F(\boldsymbol{\sigma}_{n+1}) \\ F(\boldsymbol{\sigma}_{n+1}) &\leq 0, \Delta \lambda_{n+1} F(\boldsymbol{\sigma}_{n+1}) = 0, \Delta \lambda_{n+1} \geq 0 \end{aligned} \quad (47)$$

which are the governing equations for an elastoplastic boundary value problem with an associated version of the simple elastic/perfectly plastic model (11).

Next, a mixed stress–displacement finite element approximation is introduced:

$$\boldsymbol{\sigma}(\mathbf{x}) \approx N_\sigma(\mathbf{x}) \hat{\boldsymbol{\sigma}}, \quad \mathbf{u}(\mathbf{x}) \approx N_u(\mathbf{x}) \hat{\mathbf{u}} \quad (48)$$

where the stresses are approximated in terms of shape functions $N_\sigma(\mathbf{x})$ and nodal stresses $\hat{\boldsymbol{\sigma}}$ whereas the displacement is approximated in terms of a separate set of shape functions $N_u(\mathbf{x})$ and nodal displacements $\hat{\mathbf{u}}$. Typically, the approximate displacements are continuous and differentiable inside the elements and continuous between elements, whereas the approximate stresses are continuous and differentiable inside the elements and discontinuous between elements. Standard displacement finite elements, with N_u being one polynomial order higher than N_σ , fall within this scope.

Inserting the above approximations into the spatially continuous variational principle (46) and enforcing the yield condition at a finite number of points (typically the Gauss points), we obtain the following fully discrete problem:

$$\begin{aligned} \min_{\hat{\mathbf{u}}_{n+1}} \max_{\hat{\boldsymbol{\sigma}}_{n+1}} & -(\hat{\boldsymbol{\sigma}}_{n+1} - \hat{\boldsymbol{\sigma}}_n)^\top \mathbf{C}^e (\hat{\boldsymbol{\sigma}}_{n+1} - \hat{\boldsymbol{\sigma}}_n) + (\hat{\mathbf{u}}_{n+1} - \hat{\mathbf{u}}_n)^\top (\mathbf{B}^\top \hat{\boldsymbol{\sigma}}_{n+1} - \mathbf{p}) \\ \text{subject to} & F(\hat{\boldsymbol{\sigma}}_{n+1}^j) \leq 0, j = 1, \dots, n_\sigma \end{aligned} \quad (49)$$

where

$$\mathbf{C}^e = \int_V N_\sigma^\top \mathbb{C}^e N_\sigma \, dV; \quad \mathbf{B}^\top = \int_V \mathbf{B}_u^\top N_\sigma \, dV; \quad \mathbf{p} = \int_V N_u^\top \mathbf{b} \, dV + \int_S N_u^\top \mathbf{t} \, dV \quad (50)$$

with $\mathbf{B}_u = \nabla N_u$.

The ‘min’ part of this problem may be solved first to yield the reduced problem

$$\begin{aligned} \text{maximize}_{\hat{\boldsymbol{\sigma}}_{n+1}} & -\frac{1}{2}(\hat{\boldsymbol{\sigma}}_{n+1} - \hat{\boldsymbol{\sigma}}_n)^\top \mathbf{C}^e (\hat{\boldsymbol{\sigma}}_{n+1} - \hat{\boldsymbol{\sigma}}_n) \\ \text{subject to} & \mathbf{B}^\top \hat{\boldsymbol{\sigma}}_{n+1} = \mathbf{p} \\ & F(\hat{\boldsymbol{\sigma}}_{n+1}^j) \leq 0, \quad j = 1, \dots, n_\sigma \end{aligned} \quad (51)$$

where subscript j refers to the points at which the yield condition is enforced, typically the Gauss points. In solving this problem using standard methods [14, 18, 25–27], the displacement increments are recovered as the dual variables (or Lagrange multipliers) to the discrete equilibrium equations whereas the plastic multipliers appear as the dual variables to the yield constraints (see [13] for details).

For the present application to nonassociated plasticity using the apparent cohesion approach, the only modification required is that the approximate yield function is enforced:

$$\begin{aligned} \text{maximize}_{\hat{\boldsymbol{\sigma}}_{n+1}} & -\frac{1}{2}(\hat{\boldsymbol{\sigma}}_{n+1} - \hat{\boldsymbol{\sigma}}_n)^\top \mathbf{C}^e (\hat{\boldsymbol{\sigma}}_{n+1} - \hat{\boldsymbol{\sigma}}_n) \\ \text{subject to} & \mathbf{B}^\top \hat{\boldsymbol{\sigma}}_{n+1} = \mathbf{p} \\ & F_{n+1}^*(\hat{\boldsymbol{\sigma}}_{n+1}^j) \leq 0, \quad j = 1, \dots, n_\sigma \end{aligned} \quad (52)$$

where F_{n+1}^* is calculated according to (16) at the beginning of each time step.

4.3.1. Second-order cone programming. The mathematical program (52) may be solved using general methods of mathematical programming (e.g., [25–27, 32, 33]). Using such methods, there are no restrictions on the yield inequalities. Alternatively, some generality may be sacrificed to arrive at more specialized formulations that offer increased numerical efficiency and robustness. One such possibility is to cast the problem as a second-order cone program (SOCP). The yield inequalities here must be in the form of second-order cones, which in reality limits the relevant yield criteria to those of the Drucker–Prager type. SOCPs are often cast in the following standard form [34, 35]:

$$\begin{aligned} & \text{minimize} && \mathbf{c}^\top \mathbf{x} \\ & \text{subject to} && \mathbf{A} \mathbf{x} = \mathbf{b} \\ & && \mathbf{x} \in \mathcal{K} \end{aligned} \quad (53)$$

where \mathcal{K} are second-order cones. It is noted that although the original problem (52) involves a quadratic objective function, the objective function of the SOCP standard form (53) is linear. However, by a suitable transformation, the original problem can be formulated in SOCP standard form (see Appendix A). In the present work, the final SOCPs are solved using an algorithm, SONIC, recently developed by the authors. This algorithm, which employs a homogeneous primal-dual interior-point method, will be documented in detail elsewhere. A Windows executable of SONIC is available from the corresponding author.

5. ULTIMATE LIMIT LOADS FOR NONASSOCIATED PLASTICITY

Although the assumption of an associated flow rule in many cases is questionable from a physical point of view, it does lead to a mathematically elegant theory. One of the most important outcomes in this regard is the possibility to formulate the governing equations in terms of a variational principle. The upper-bound and lower-bound theorems, which enable the exact collapse load of a structure of perfectly plastic materials to be bracketed from above and below, are prominent examples of such principles. However, the assumption of associated flow is crucial to these principles, and efforts to extend them to cover nonassociated flow have largely been futile. Indeed, a long-standing question, particularly in soil mechanics, is to what extent the flow rule influences the bearing capacity of typical structures such as foundations, slopes, and retaining walls. Although some efforts have been made to settle the question numerically [7, 10, 36–39], these have often been hampered by the poor performance of conventional solution schemes as discussed in Section 1.

Another approach was suggested by Drescher and Detournay [40] who, on the basis of the previous work of Davis [41], advocated the use of conventional limit analysis in conjunction with ‘effective’ material parameters, the magnitude of which depends on the degree of nonassociativity. In the following, we consider a similar approach and derive effective parameters for the Drucker–Prager criterion. However, it is also shown that although these parameters in many cases yield reasonable estimates, they cannot be used to rigorously bracket the limit load from above or below.

5.1. Localized states of deformation

The elastic limit for a nonassociated elastoplastic model of the type (11) is given solely in terms of the yield function F . As such, the elastic stress states that can be attained are in principle independent of the flow rule. However, during plastic flow, the flow rule has an impact on the way in which internally or externally imposed kinematic constraints affect the overall behavior. This is particularly the case when the mode of deformation is localized. In the following, we consider a situation where a homogeneous state of stress and strain gives way, gradually or suddenly, to a localized state of deformation as exemplified by the biaxial test sketched in Figure 5.

The stresses in the shear band satisfy the yield criterion (3), which in the n – t coordinate system shown in Figure 5 reads

$$F = \sqrt{\frac{1}{2}(\sigma_n - \sigma_t)^2 + \frac{1}{2}(\sigma_n - \sigma_2)^2 + \frac{1}{2}(\sigma_2 - \sigma_t)^2 + 3\tau_{nt}^2} + M(\sigma_n + \sigma_t + \sigma_2) - k \leq 0 \quad (54)$$

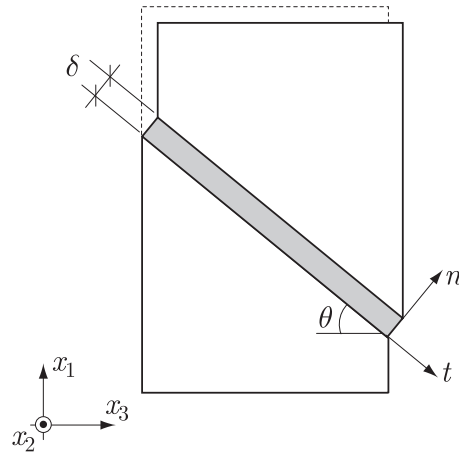


Figure 5. Plane strain localization.

whereas the plastic potential is given by

$$G = \sqrt{\frac{1}{2}(\sigma_n - \sigma_t)^2 + \frac{1}{2}(\sigma_n - \sigma_2)^2 + \frac{1}{2}(\sigma_2 - \sigma_t)^2 + 3\tau_{nt}^2} + N(\sigma_n + \sigma_t + \sigma_2) \quad (55)$$

For a shear band, or plane, of width δ tending to zero, the normal strain parallel to the plane also tends to zero (relative to the normal strain perpendicular to the plane). This effectively imposes the following conditions on the stresses

$$\begin{aligned} \dot{\varepsilon}_t^p = \dot{\lambda} \frac{\partial G}{\partial \sigma_t} = 0 &\implies \sigma_t = \frac{1}{2}(\sigma_n + \sigma_2) - \frac{\sqrt{3}N}{2\sqrt{9-N^2}} \sqrt{(\sigma_n - \sigma_2)^2 + 4\tau_{nt}^2} \\ \dot{\varepsilon}_2^p = \dot{\lambda} \frac{\partial G}{\partial \sigma_2} = 0 &\implies \sigma_2 = \frac{1}{2}(\sigma_n + \sigma_t) - \frac{\sqrt{3}N}{2\sqrt{9-N^2}} \sqrt{(\sigma_n - \sigma_t)^2 + 4\tau_{nt}^2} \end{aligned} \quad (56)$$

The solution to these equations is given by

$$\sigma_t = \sigma_2 = \sigma_n - \frac{2\sqrt{3}N}{\sqrt{9-4N^2}} |\tau_{nt}| \quad (57)$$

Inserting this into the original yield function (54) gives the effective strength domain for the shear band:

$$f_{loc} = |\tau_{nt}| + \frac{\sqrt{9-4N^2}}{9-4MN} \sqrt{3}M\sigma_n - \frac{\sqrt{9-4N^2}}{9-4MN} \sqrt{3}k \leq 0 \quad (58)$$

which may also be written as

$$f_{loc} = |\tau_{nt}| + \frac{\sqrt{3}M_{loc}}{\sqrt{9-4M_{loc}^2}} \sigma_n - \frac{\sqrt{3}k_{loc}}{\sqrt{9-4M_{loc}^2}} \leq 0 \quad (59)$$

where

$$M_{loc} = \omega_{loc}M, k_{loc} = \omega_{loc}k; \omega_{loc} = \sqrt{\frac{9-4N^2}{9+4M^2-8MN}} \quad (60)$$

Alternatively, in terms of the equivalent Mohr–Coulomb parameters (5), the effective yield function is given by

$$f_{loc} = |\tau_{nt}| + \sigma_n \tan \phi_{loc} - c_{loc} \quad (61)$$

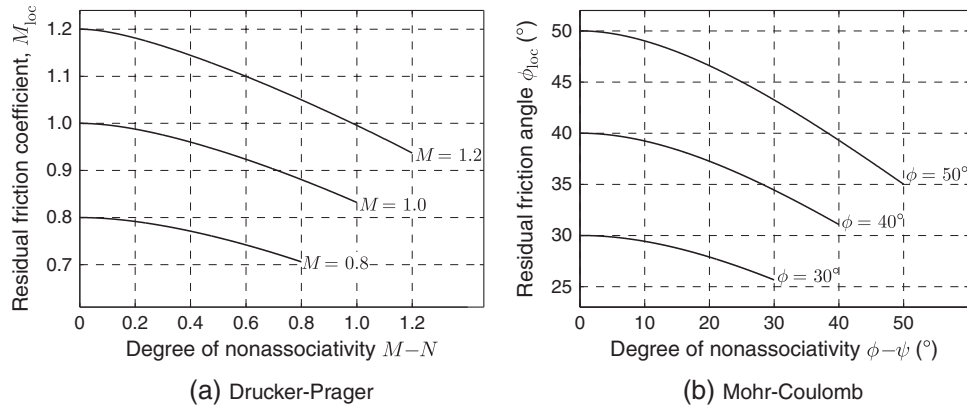


Figure 6. Effective friction parameters as function of degree of nonassociativity: (a) Drucker–Prager and (b) equivalent plane strain Mohr–Coulomb.

where ϕ_{loc} and c_{loc} are related to M_{loc} and k_{loc} by relations equivalent to (5), namely

$$M_{loc} = \frac{3 \sin \phi_{loc}}{\sqrt{3 + \sin^2 \phi_{loc}}}, k_{loc} = \frac{3 \cos \phi_{loc}}{\sqrt{3 + \sin^2 \phi_{loc}}} c_{loc} \tag{62}$$

Furthermore, M_{loc} and k_{loc} are related to N , and thereby to ψ , by (60). The effects of the degree of nonassociativity in terms of reduction in the effective material parameters are shown in Figure 6(a) for the Drucker–Prager criterion and in Figure 6(b) for the equivalent Mohr–Coulomb criterion. These reduced parameters imply a potentially significant decrease in the load bearing capacity of nonassociated plastic structures.

It should be borne in mind, however, that the effective yield function f_{loc} (61) only gives a relation between the normal and shear strains in a localized band of deformation undergoing yielding. In the associated case, the variational principles of classical plasticity theory guarantee that these stresses as well as the shear band orientation are such that the global load bearing capacity is at an optimum. However, in the nonassociated case, these principles are no longer valid, and besides the relation between shear and normal stresses expressed by f_{loc} , no general statements about the conditions at the ultimate limit state can be made. In this way, the approach of Drescher and Detournay [40] of deriving ‘nonassociated limit loads’ by using the effective strength parameters in an associated framework also appears somewhat questionable and, in any case, not generally valid. Indeed, although the approach in many cases provide reasonable estimates of the residual bearing capacity, these estimates may be either conservative and unconservative depending on the particular problem. Examples of both types of scenarios are given by Section 6. Moreover, the Drescher and Detournay approach does not address the important fact that the use of a nonassociated flow rule in general leads to boundary value problems that are ill-posed. This ill-posedness manifests itself in non-uniqueness of solutions (making it questionable to refer to *the* limit load in analogy with associated plasticity) and a possible pathological sensitivity to the boundary conditions, the initial stress state, and so on. These issues are discussed in more detail in the following section.

5.2. Onset of localization and post-bifurcation behavior

The onset of shear banding can be gauged by the determinant of the acoustic tensor:

$$\mathbf{Q} = \mathbf{N}^T \mathbb{D}^{ep} \mathbf{N} \tag{63}$$

where \mathbb{D}^{ep} is the elastoplastic constitutive modulus and $\mathbf{N}^T = \nabla^T(\mathbf{n}\mathbf{x}^T)$ with $\mathbf{n} = (n_1, n_2, n_3)^T$ being the normal to the shear plane. Following [1–6], it can be shown that a non-positive determinant of \mathbf{Q} coincides with the possibility of switching from a homogeneous to a localized mode of deformation.

With reference to the biaxial test sketched in Figure 5, a bifurcation analysis can be carried out by gradually increasing the vertical load while gauging the smallest value of $\det(\mathbf{Q})$ in each time step. That is, in each step, the determinant of \mathbf{Q} is computed for the entire range of potential shear band orientations as given by the inclination angle θ . Once a minimum value of $\det[\mathbf{Q}(\theta = \theta_{loc})] = 0$ is attained, a localized mode of deformation given in terms of a shear band with inclination angle $\theta = \theta_{loc}$ is possible. However, the critical angle for which localization first becomes possible in general does not coincide with the angle for which the smallest residual strength is attained. Indeed, as the acoustic tensor depends on the elastic moduli, the critical shear band angle will in general depend on the elastic constants. Thus, even though the stresses in the shear band satisfy the reduced strength criterion $f_{loc} = 0$ as given by (61), the inclination of the shear band need not be optimal in the sense that the smallest possible residual load is attained—except in the case of an associated flow rule where this angle coincides with the one that leads to a zero determinant of the acoustic tensor. Moreover, although a zero determinant of the acoustic tensor indicates the possibility of localization, it does not necessitate it. Indeed, a continued homogeneous state of deformation is equally likely. If this path is followed beyond the point where $\det(\mathbf{Q}) = 0$, there will usually be a range of inclination angles for which $\det(\mathbf{Q}) \leq 0$. In this way, the localized mode of deformation becomes non-unique as not one but a range of solutions are possible, each resulting in a different ultimate limit load.

These features have a tendency to make finite element solutions to general boundary value problems rather strongly dependent on the structure and orientation of the mesh. Moreover, it is often observed that a switch between different modes of localized deformation takes place, eventually resulting in somewhat oscillatory load–deformation curves. These characteristics are discussed by way of example in the next section.

6. EXAMPLES

In the following, a number of examples demonstrating the capabilities of the new schemes and highlighting the effects of nonassociativity are presented.

6.1. Biaxial test

The first example concerns the biaxial test shown in Figure 7. The horizontal stress is zero whereas the vertical stress, σ_c , is induced by a rigid and perfectly smooth end platen. Assuming associated flow and a collapse mechanism defined by a single shear band with inclination θ as shown in Figure 5, an upper bound on the limit load is given by

$$\sigma_c = \frac{c \cos \phi}{\sin(\theta - \phi) \cos \theta} \quad (64)$$

where c and ϕ are related to k and M by (5). The optimal value of θ , that is, the value implying the smallest upper bound, is given by $\theta = 45^\circ + \frac{1}{2}\phi$, resulting in

$$\sigma_c = 2c \tan(45^\circ + \frac{1}{2}\phi) \quad (65)$$

Following the argumentation of the previous section, the same kind of single-band mechanism is also valid for the case of nonassociated flow. The ultimate limit load corresponding to such a localized solution is given by

$$\sigma_{c,loc} = \frac{c_{loc} \cos \phi_{loc}}{\sin(\theta - \phi_{loc}) \cos \theta} \quad (66)$$

where the smallest value of σ_c is obtained for $\theta = 45^\circ + \frac{1}{2}\phi_{loc}$.

In the numerical analysis of the problem, three different meshes as shown in Figure 7(a–c) are used. These meshes have particular properties attached to them. Mesh (a) is optimal in the sense that its diagonals are aligned along the shear band inclination that leads to the lowest limit load, that is, $\theta = 45^\circ + \frac{1}{2}\phi_{loc} = 62.2^\circ$ (where $\phi_{loc} = 34.4^\circ$ corresponding to $\phi = 40^\circ$ and $\psi = 10^\circ$). The diagonals of mesh (b) are aligned along the shear band angle approximately corresponding to the point

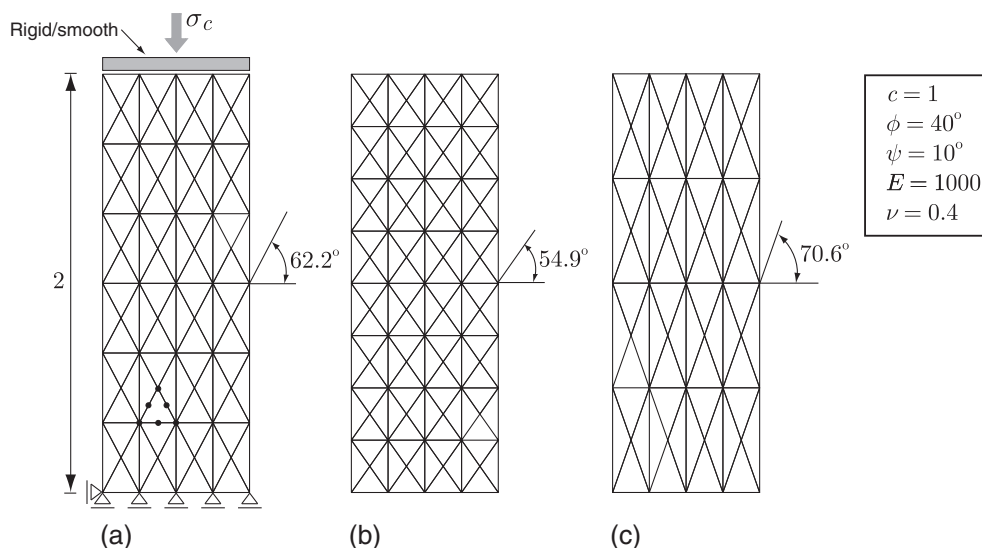


Figure 7. Biaxial test: optimal (a) and suboptimal (b, c) mesh arrangements for $\phi = 40^\circ$ and $\psi = 10^\circ$ (coarse meshes).

where localization first becomes possible according to the criterion that $\det(\mathbf{Q}) = 0$. This angle is given by $\theta_{\text{loc,init}} \simeq 55.6^\circ$. If homogenous deformation is continued beyond this point, localization will eventually be possible along a range of shear band orientations. At the ultimate limit state, this range is

$$50^\circ \leq \theta_{\text{loc,ult}} \leq 62.6^\circ \quad (67)$$

In the inclination of the diagonals of mesh (c), 70.6° falls outside this range of possible shear band angles. Thus, even though localization via a shear band inclination angle of $\theta = 70.6^\circ$ would lead to a limit load well below the associated limit load, we should expect that such a localization will not take place. For all meshes used, an element located approximately at the center of the block is assigned a reduced stiffness in order to trigger localization.

The results of the numerical analyses are shown in Figures 8 and 9. Firstly, in Figure 8, the results for three different meshes of type (a) are shown. The coarse mesh [shown in Figure 7(a)] contains 128 six-node quadratic displacement elements, whereas the medium and fine meshes contain 512 and 2048 such elements, respectively. The load–displacement curves all display a peak before tending to the expected residual level as given by (66) for $\phi_{\text{loc}} = 34.4^\circ$. It is also seen that the bifurcation, as indicated by an apparent softening, occurs somewhat earlier than the analytical bifurcation analysis suggests, which can be explained by the presence of the imperfection.

Secondly, in Figure 9, the load–displacement curves for the fine versions of meshes (a), (b), and (c) are shown. It is observed here that the residual load for mesh (b) is slightly higher than that associated with mesh (a) and in fact corresponds approximately to that predicted by (66), assuming a localization angle equal to the inclination angle of the mesh, that is, $\theta = 54.9^\circ$.

The patterns of plastic deformation shown in Figure 10 support these findings. Firstly, for mesh (a), a shear band coinciding exactly with the diagonals of the mesh is observed. For mesh (b), the same kind of pattern is initially observed after which a second band develops. The development of this second band corresponds to the slight increase in stiffness observed at a displacement of $u \simeq 0.02$ in Figure 9. This switching between slightly different modes of failure and a corresponding oscillatory load–deformation behavior is quite typical of general boundary value problems as will be demonstrated by the following examples. The phenomenon has also been noted and studied in some detail by Nordal [42]. Furthermore, for a model considerably more complex than the present one, Gajo *et al.* [43] found this type of switching between different failure modes well beyond the initial point of failure to be an integral part of the underlying constitutive model. Their results were

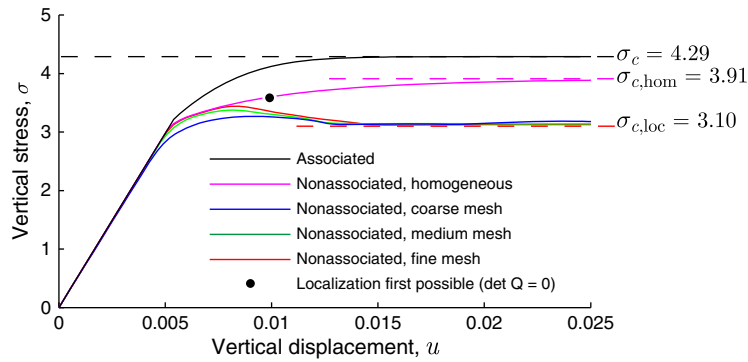


Figure 8. Biaxial test: solutions for coarse, medium, and fine meshes of type (a).

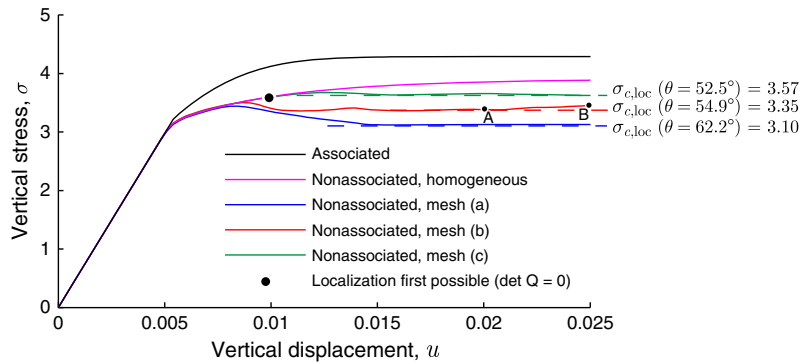


Figure 9. Biaxial test: solutions for fine meshes of types (a), (b), and (c).

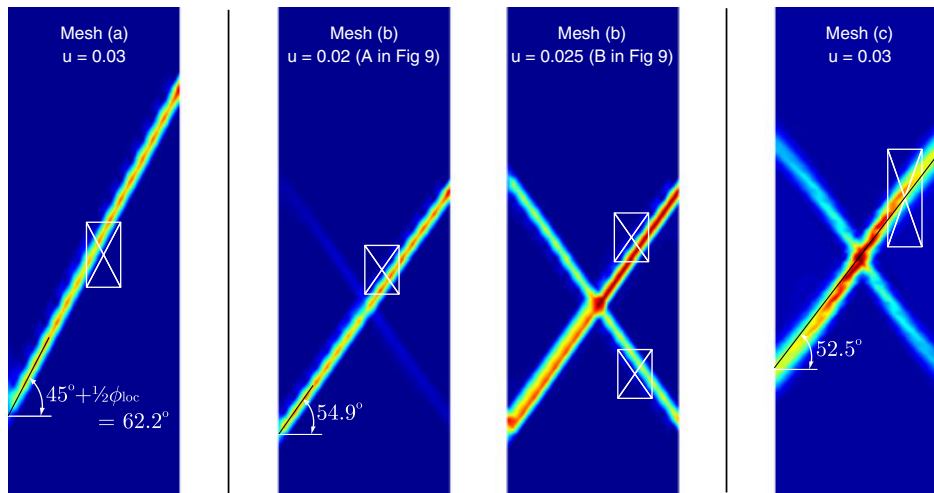


Figure 10. Biaxial test: rate of plastic shear strain for meshes (a) and (b). The shear bands follow the diagonals of the meshes in cases (a) and (b), but not in case (c).

further related to experimental data for dense sands displaying similar characteristics. There is thus some indication that the oscillatory load–deformation behavior observed in the numerical solution of boundary value problems represents real physics rather than a mathematical pathology.

Finally, for mesh (c), a still higher residual load is observed, corresponding approximately to a shear band inclination angle of $\theta \simeq 52.5^\circ$ for which $\sigma_c = 3.57$. It is worth noting here that the shear band does not follow the diagonals of the mesh as in the previous examples. This is in line

with the analytical bifurcation analysis although, from the point of view that the mesh arrangement favors a shear band inclined at $\theta = 70.6^\circ$, it is somewhat surprising. Moreover, the residual load associated with this inadmissible mechanism is somewhat lower than that actually found, that is, $\sigma_c = 3.44$ versus $\sigma_c = 3.57$, and well below the limit load associated with the homogenous solution. In fact, the range of shear band inclination angles for which the residual load is lower than for homogenous mode of failure is given by $50^\circ \leq \theta \leq 74.4^\circ$, although only part of this range, namely $50^\circ \leq \theta \leq 62.6^\circ$, is admissible according to the bifurcation analysis. The requirement that the mechanism is admissible from a bifurcation point of view, that is, that it is possible to switch from a homogenous to a localized mode of failure, may give rise to the somewhat paradoxical situation that the angle, which results in the lowest residual load, $\theta = 45 + \frac{1}{2}\phi_{loc}$, is outside the admissible range of shear band inclination angles. Indeed, for $\nu = 0.3$ (instead of $\nu = 0.4$ as used in the present analyses), the admissible range is $50^\circ \leq \theta \leq 61.6^\circ$ so that the most critical failure mechanism, namely that defined by $\theta = 45^\circ + \frac{1}{2}\phi_{loc} = 62.2^\circ$, is inadmissible. In this case, the use of the reduced material parameters in an associated setting as suggested by Drescher and Detournay would lead to an underestimate of the actual residual load.

Regarding the performance of the three algorithms, the implicit schemes (standard and with apparent cohesion interpretation) both performed relatively well, using typically three to five iterations per time step to attain convergence to within a tolerance of 10^{-8} . In contrast, the second-order cone programming algorithm requires some 20–30 iterations per time step, independent of the magnitude of the time step, the proximity to the residual state, and so on. It should be noted, however, that the biaxial test is a relatively uncomplicated example. More challenging examples will be presented in the following sections.

6.2. Strip footing

The next example concerns the classic strip footing problem sketched in Figure 11. The bearing capacity of a rigid strip footing subjected to a central vertical load is usually expressed as

$$V/B = cN_c + \frac{1}{2}B\gamma N_\gamma \quad (68)$$

where V is the vertical force per unit length of the footing into the plane, B is the footing width, γ is the unit weight, and N_c and N_γ are bearing capacity factors that depend on the frictional angle of the material. For the problem where $\gamma = 0$, N_c can be determined as

$$N_c = [\tan^2(45^\circ + \frac{1}{2}\phi)e^{\pi \tan \phi} - 1] \cot \phi \quad (69)$$

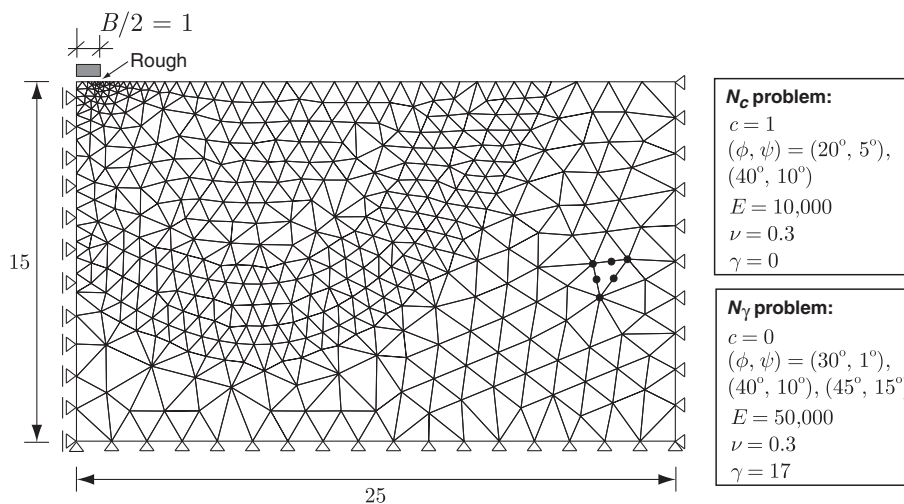


Figure 11. Strip footing: problem setup and finite element mesh (coarse).

This result is originally by Prandtl [44]. Conversely, for $c = 0$, Hjjaj *et al.* [45] have determined an approximate expression for N_γ given by

$$N_\gamma = e^{\frac{1}{6}(\pi + 3\pi^2 \tan \phi)} \tan^{\frac{2}{3}\pi} \phi \quad (70)$$

In the following, these two types of problems, involving first a weightless cohesive-frictional material and then a ponderable purely frictional material, are considered. In all cases, 200 vertical displacement increments of equal magnitude are enforced on the footing. The three different methods of solution presented in Section 4 are employed: the standard implicit scheme, the modified implicit scheme utilizing the apparent cohesion interpretation, and the mathematical programming formulation in conjunction with the second-order cone programming solver SONIC. Although the latter scheme always produces a solution for a given time step, the two former may occasionally fail to converge. If this happens, the time step is halved and then, in the subsequent steps, gradually increased by 25% until the original step size is attained. Regarding the relative efficiency of the different schemes, the total number of iterations used appears to be the most objective measure. In the two implicit schemes, the majority of the computational effort is spent on the global equilibrium iterations involving the factorization of the tangent stiffness matrix. In the mathematical programming formulation, each iteration involves the solution of a similar set of linear equations. However, when comparing total iteration counts (Tables II and III), it should be noted that only successful iterations are counted. This creates some bias against the mathematical programming formulation, which in some cases may be significantly more efficient than it appears.

6.2.1. N_c problem. The results for the two different N_c problems are shown in Figure 12. Firstly, in Figure 12(a), the results for a material with $\phi = 20^\circ$ and $\psi = 5^\circ$ are shown. As seen, the results of the standard implicit and the apparent cohesion schemes are for all practical purposes identical. Moreover, the rather moderate degree of nonassociativity leads to load–displacement responses that are relatively smooth and free of oscillations.

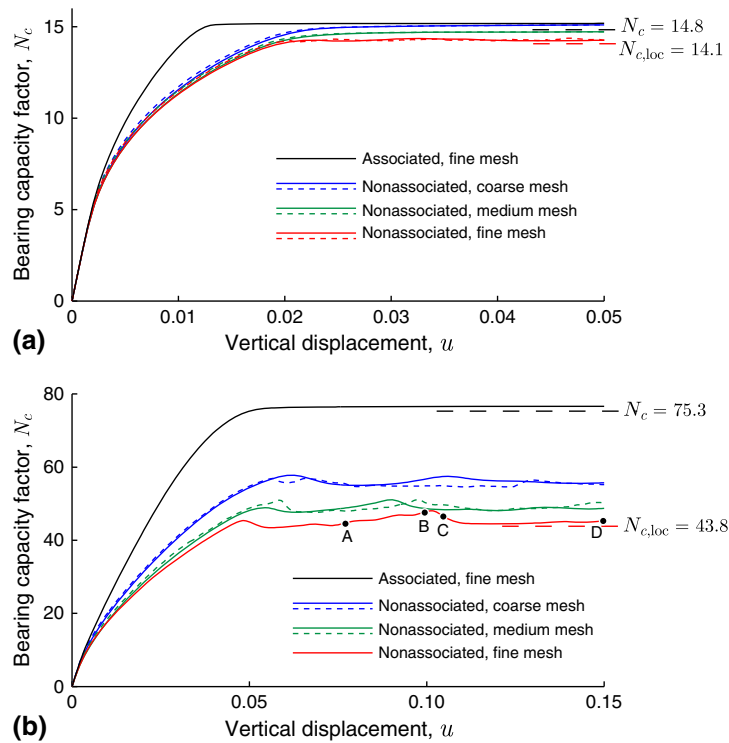
However, by increasing the degree of nonassociativity, such oscillations do appear. In Figure 12(b), the results for a material with $\phi = 40^\circ$ and $\psi = 10^\circ$ are shown. Again, the two different methods of solution produce similar load–displacement responses, particularly up to the point where oscillations begin to appear. As mentioned previously, these oscillations are a consequence of the ill-posedness of the boundary value problem and correspond physically to a switching between different modes of failure beyond the point at which the load carrying capacity of the structure first becomes exhausted. This is illustrated in Figure 13 where it is seen that the failure modes change quite significantly between different time steps beyond the point at which the limit load apparently is reached (in this case, at a displacement of $u \simeq 0.05$). In all cases, use of the reduced parameters, ϕ_{loc} and c_{loc} , in a classical associated limit analysis setting furnishes reasonable estimates of the residual bearing capacity (these values are indicated by $N_{c,\text{loc}}$ in Figure 12).

Table II. N_c problem: solution statistics for the standard implicit scheme (Section 4.1), the new implicit apparent cohesion scheme (Section 4.2), and the mathematical programming scheme (Section 4.3).

| | Coarse mesh | | | Medium mesh | | | Fine mesh | | |
|--|-------------|-----------------|-----------------|-------------|-----------------|-----------------|------------|-----------------|-----------------|
| | Std. impl. | Eff. coh. impl. | Eff. coh. SONIC | Std. impl. | Eff. coh. impl. | Eff. coh. SONIC | Std. impl. | Eff. coh. impl. | Eff. coh. SONIC |
| Case (a): $\phi = 20^\circ$, $\psi = 5^\circ$. Results are shown in Figure 12(a). | | | | | | | | | |
| Time steps | 200 | 200 | 200 | 200 | 200 | 200 | 616 | 200 | 200 |
| Iterations | 646 | 828 | 5246 | 712 | 1134 | 4824 | 5678 | 1518 | 5300 |
| Iter. ratio | 0.78 | 1.00 | 6.34 | 0.63 | 1.00 | 4.25 | 3.74 | 1.00 | 3.49 |
| Case (b): $\phi = 40^\circ$, $\psi = 10^\circ$. Results are shown in Figure 12(b). | | | | | | | | | |
| Time steps | 215 | 200 | 200 | 427 | 200 | 200 | Failed | 200 | 200 |
| Iteration | 1014 | 1260 | 4680 | 1878 | 1337 | 4565 | – | 1560 | 4846 |
| Iter. ratio | 0.80 | 1.00 | 3.71 | 1.40 | 1.00 | 4.25 | – | 1.00 | 3.10 |

Table III. N_γ problem: solution statistics for the standard implicit scheme (Section 4.1), the new implicit apparent cohesion scheme (Section 4.2), and the mathematical programming scheme (Section 4.3).

| | Coarse mesh | | | Medium mesh | | | Fine mesh | | |
|--|-------------|-----------------|-----------------|-------------|-----------------|-----------------|------------|-----------------|-----------------|
| | Std. impl. | Eff. coh. impl. | Eff. coh. SONIC | Std. impl. | Eff. coh. impl. | Eff. coh. SONIC | Std. impl. | Eff. coh. impl. | Eff. coh. SONIC |
| Case (a): $\phi = 30^\circ$, $\psi = 1^\circ$. Results are shown in Figure 15(a). | | | | | | | | | |
| Time steps | 202 | 202 | 200 | 200 | 204 | 200 | Failed | 666 | 200 |
| Iterations | 567 | 948 | 5464 | 664 | 1089 | 4864 | – | 7996 | 5145 |
| Iter. ratio | 0.60 | 1.00 | 5.76 | 0.61 | 1.00 | 4.47 | – | 1.00 | 0.64 |
| Case (b): $\phi = 40^\circ$, $\psi = 10^\circ$. Results are shown in Figure 15(b). | | | | | | | | | |
| Time steps | 218 | 200 | 200 | Failed | 200 | 200 | Failed | 315 | 200 |
| Iterations | 783 | 1607 | 4425 | – | 1964 | 5049 | – | 6625 | 5124 |
| Iter. ratio | 0.49 | 1.00 | 2.75 | – | 1.00 | 5.57 | – | 1.00 | 0.77 |
| Case (c): $\phi = 45^\circ$, $\psi = 15^\circ$. Results are shown in Figure 15(c). | | | | | | | | | |
| Time steps | Failed | 200 | 200 | Failed | 202 | 200 | Failed | 556 | 200 |
| Iterations | – | 1459 | 4711 | – | 2851 | 4782 | – | 12,343 | 5295 |
| Iter. ratio | – | 1.00 | 3.23 | – | 1.00 | 1.68 | – | 1.00 | 0.43 |

Figure 12. N_c problem: load–displacement curves for (a) $\phi = 20^\circ$, $\psi = 5^\circ$ and (b) $\phi = 40^\circ$, $\psi = 10^\circ$. Dashed curves correspond to the standard implicit scheme and full curves to the new apparent cohesion scheme.

The performance of the different solution schemes is summarized in Table I. Several conclusions can be drawn from these statistics. Firstly, in cases where the degree of nonassociativity is moderate and the mesh is relatively coarse, the standard implicit scheme outperforms the other two as measured by the total number of successful iterations. However, when the degree of nonassociativity increases or the mesh is refined, the new apparent cohesion scheme becomes more efficient.

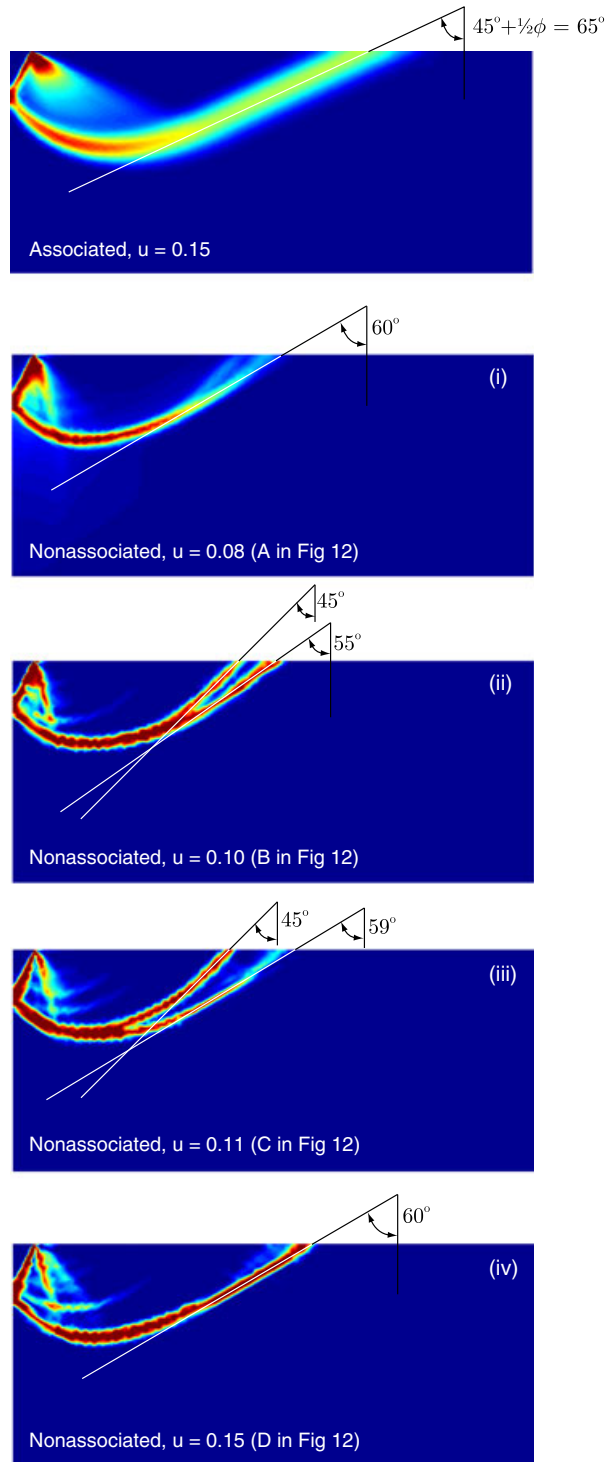


Figure 13. Strip footing (N_c problem): rate of plastic shear strain at different times for $\phi = 40^\circ$, $\psi = 10^\circ$. The optimal shear band inclination angle in the nonassociated case is $45^\circ + \frac{1}{2}\phi_{loc} = 62.2^\circ$.

Indeed, for the finest mesh with $\phi = 40^\circ$ and $\psi = 10^\circ$, the standard scheme fails in the sense that the time steps required for convergence becomes prohibitively small. Finally, although the use of a mathematical programming formulation in conjunction with the second-order cone programming

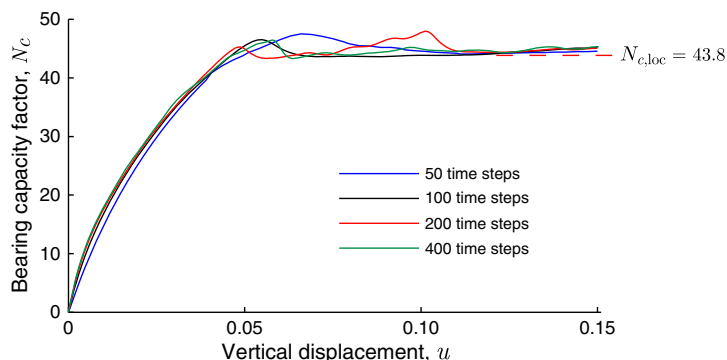


Figure 14. N_c problem with $\phi = 40^\circ$, $\psi = 10^\circ$: Influence of time discretization for fine mesh using the apparent cohesion scheme.

solver SONIC is by far the most robust scheme, it is somewhat more expensive than the conventional implicit schemes, although the gap is narrowed as the problems become more challenging, that is, as the mesh density and degree of nonassociativity increase.

Regarding the effect of the time discretization, it can be seen from Figure 14 that the results are relatively insensitive to the magnitude of the time step and appear to converge rather quickly, at least in the pre-bifurcation regime. Moreover, it is also observed that the oscillatory load–displacement behavior previously discussed is unaffected by the magnitude of the time step. In fact, if anything, smaller time steps tend to produce more oscillatory responses than larger ones.

6.2.2. N_γ problem. We now turn our attention to the N_γ problem. Even in the associated case, this problem is known to be significantly more challenging than the N_c problem (see, e.g., [14]). Three different sets of material parameters are considered: (a) $\phi = 30^\circ$, $\psi = 1^\circ$, (b) $\phi = 40^\circ$, $\psi = 10^\circ$, and (c) $\phi = 45^\circ$, $\psi = 15^\circ$. These parameter sets, which correspond approximately to loose, medium, and dense sand, represent an increase in the degree of nonassociativity and thereby, it is expected in the degree of difficulty.

The load–displacement curves corresponding to the three different parameter sets are shown in Figure 15. As with the N_c problem, a somewhat oscillatory behavior is observed, especially for dense meshes and large degrees of nonassociativity. However, in contrast to the N_c problem, the effective friction angle associated with fully localized solutions, ϕ_{loc} , does not furnish particularly good estimates of the residual load. The computed nonassociated residual loads are, however, well below those of the equivalent associated limit loads. Indeed, for case (c), the limit load is almost halved. The reasons for the poor performance of the effective parameter approach of Drescher and Detournay is to be found in the collapse mechanism as shown in Figure 16. Although the normal and shear stresses in the localized zones do satisfy the effective yield criterion (61), there is no guarantee that the resulting pattern of localized deformation is optimal in the sense that it produces the lowest possible collapse load. Indeed, although the optimal mechanism would be expected to show the major shear band forming an angle of $45^\circ + \frac{1}{2}\phi_{loc} = 62.2^\circ$ with the vertical, the angle actually observed is closer to $45^\circ + \frac{1}{2}\psi = 50^\circ$. The performance of the various solution schemes is summarized in Table II. The major trends are similar to those of the N_c problem. The performance of the standard implicit scheme is particularly noteworthy in that it succeeds only for the easiest problems, that is, for the coarsest meshes and the smallest degrees of nonassociativity. In this context, it should be noted that both the physical problems and the material parameters used are quite realistic. Likewise, the finite element models are not excessively large. It is also worth noting that the mathematical programming scheme in all cases is the most efficient for the finest mesh, independent of the material parameters.

Finally, we note that the deformations, especially in cases (b) and (c), are of such a magnitude that a finite deformation formulation appears to be necessary, despite the fact that reasonable material parameters, such as geometric dimensions, have been used. In practice, such a formulation would

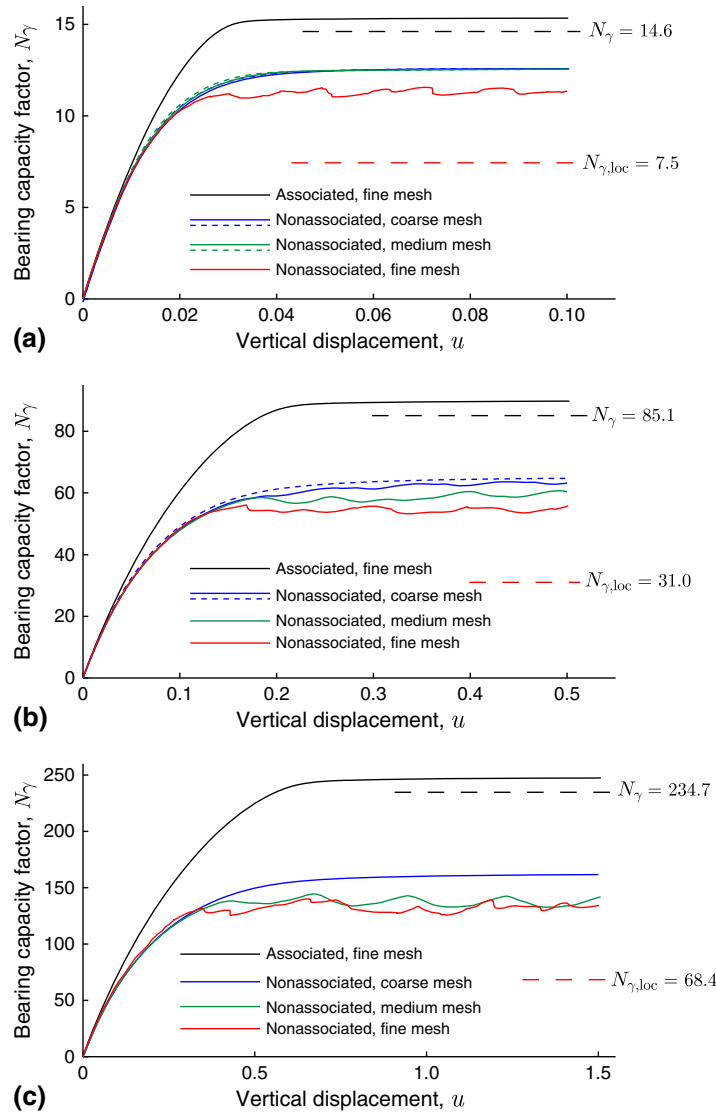


Figure 15. N_γ problem: load–displacement curves for (a) $\phi = 30^\circ$, $\psi = 1^\circ$, (b) $\phi = 40^\circ$, $\psi = 10^\circ$, and (c) $\phi = 45^\circ$, $\psi = 15^\circ$. Dashed curves correspond to the standard implicit scheme and full curves to the new apparent cohesion scheme.

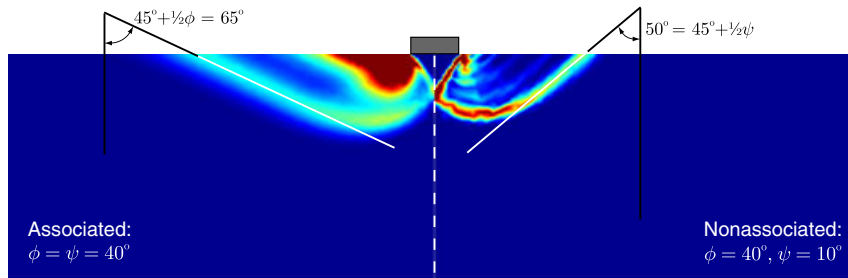


Figure 16. N_γ problem: rates of plastic shear strain at $u = 0.5$ for $\phi = 40^\circ$ and $\psi = 10^\circ$.

need to include inertial forces as the slope formed as the footing penetrates the soil will be unstable from a purely static point of view, thus preventing any further static penetration of the footing.

6.3. Anchor pull-out in a purely frictional soil

The final example concerns the pull-out of an anchor in a purely frictional soil. The anchor is subjected to a central vertical force that increases monotonically until failure. Symmetry is exploited to model half the problem as shown in Figure 17 (the actual mesh used in the calculations contains approximately 10,500 six-node elements and 42,000 displacement degrees of freedom). The soil–anchor interface is modeled using an approach previously developed for limit analysis applications [22, 46]. The basic idea is to enforce kinematically admissible velocity discontinuities between the anchor and the surrounding soil. Alternatively, such discontinuities can be viewed as comprising zero-thickness elements of the same type as those used to model the soil. In conventional finite element formulations, such zero-thickness elements would cause the stiffness matrix to become singular. Similarly, for elements with a finite but very small thickness, the stability of the global iteration scheme tends to suffer. On the other hand, the mathematical programming formulation outlined in Section 4.3 is quite insensitive to such features. In the following, therefore, this scheme is the only one used. Two different cases of soil–anchor interface conditions are considered: the perfectly rough case where the interface properties are identical to those of the soil and the perfectly smooth case where the interface friction angle is zero. The load–deformation curves for these two cases are shown in Figure 18. The load levels referred to as V_{loc}^{rough} and V_{loc}^{smooth} correspond to those obtained numerically using the corresponding effective friction angle in an associated framework following the approach of Drescher and Detournay [40]. For $\phi = 30^\circ$ and $\psi = 0^\circ$, the effective friction angle is $\phi_{loc} = 25.7^\circ$.

The load–displacement curves for the two cases, rough and smooth, are shown in Figure 18. The difference between the two in terms of the ultimate limit load is quite small—and in the nonassociated case negligible. This agrees with previous findings (e.g., [47]). As with the previous examples, a decrease in the ultimate limit load as a result of imposing a nonassociated flow rule is observed. The conditions at incipient collapse are also markedly different as shown in Figures 19 and 20. Again, the nonassociated calculation leads to a more localized pattern of deformation and to a more confined collapse mechanism.

Interestingly, however, and in contrast to the previous examples, the computed nonassociated limit loads are smaller than those obtained with the use of the reduced friction angle ϕ_{loc} in an associated framework. To our knowledge, these results are the first of their kind, at least for a reasonably

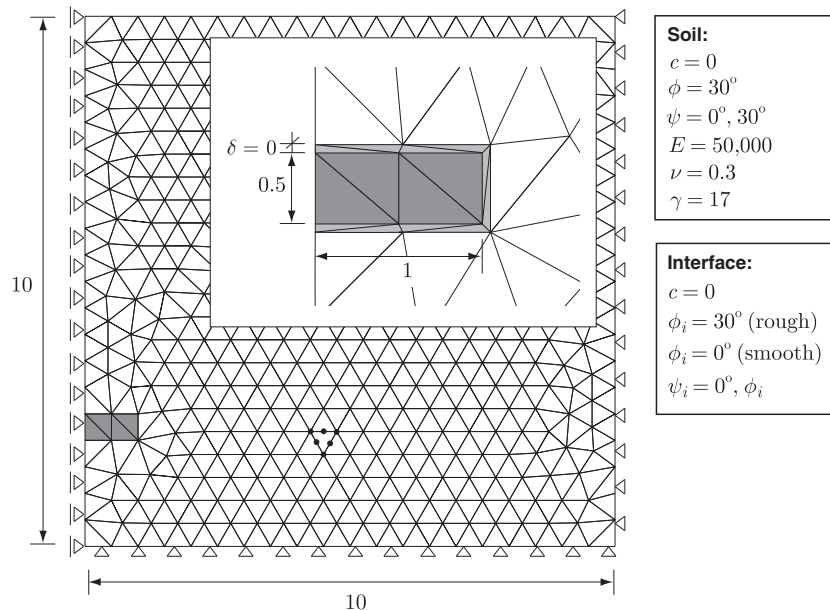


Figure 17. Anchor in purely frictional soil: problem setup and finite element mesh (coarse).

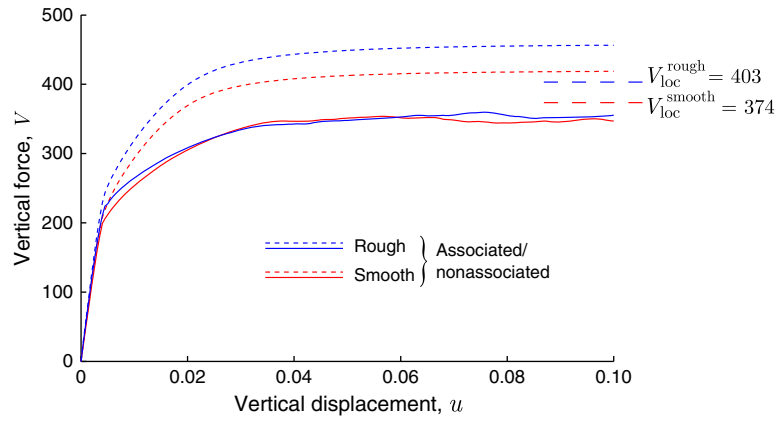


Figure 18. Anchor problem: load–displacement curves for fine mesh using 200 equal-size time steps.

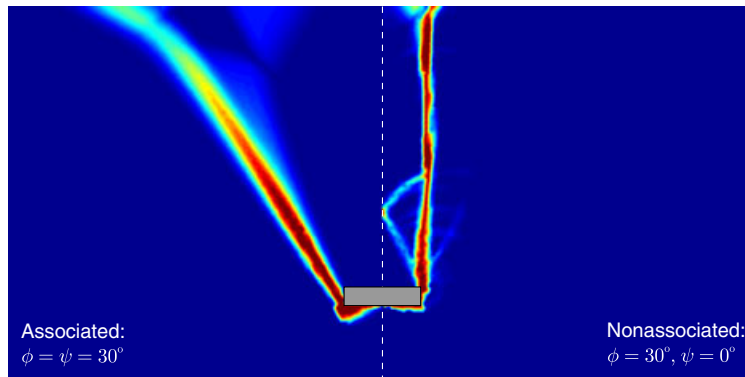


Figure 19. Anchor problem: rates of plastic shear strain at collapse.

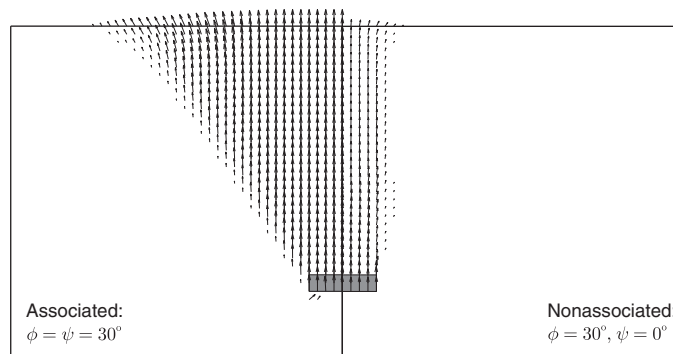


Figure 20. Anchor problem: displacements at collapse.

realistic boundary value problem. They again highlight the fact that the Drescher and Detournay approach provide an estimate of the influence of nonassociativity that, depending on the problem, may be either on the safe or on the unsafe side. Indeed, although the normal and shear stresses in the plastic zones are related by the effective yield condition $|\tau| = \sigma_n \tan \phi_{loc}$, there is no guarantee that the normal stress will attain the value necessary to ensure equivalence to an associated calculation with $\phi = \psi = \phi_{loc}$.

7. CONCLUSIONS

A new approach to computational elastoplasticity of nonassociated frictional materials has been proposed. Effectively, each time step involves the solution of an approximate associated problem. As such, methods previously developed for associated plasticity are applicable with little modification as has been demonstrated by the adaptation of the standard implicit scheme. Moreover, variational formulations that subsequently are resolved using either general or more specialized methods of mathematical programming are applicable and offer a number of advantages over more traditional schemes. However, although the physical motivation behind the new scheme is fundamentally sound and the results obtained are in good agreement with those obtained by more traditional means (in the case where these can be obtained), a formal proof of the convergence of the scheme is still lacking. In other words, the rigorous determination of the exact magnitude of the time step required to produce an acceptable solution remains to be investigated.

Regarding the numerical difficulties suffered in conventional solutions schemes, it has been shown that these are closely correlated to the appearance of spurious oscillations in the load–deformation response, which in turn are the result of spurious switching between different modes of localization. The present work, and in particular the proposed method of solution via mathematical programming, eliminates these difficulties and paves the way for rigorous studies on the effects of nonassociativity for a wide range of problems in geomechanics and elsewhere. Although such studies have been attempted on a number of occasions, the numerical methods available have in practice often limited the scope to moderate degrees of nonassociativity and rather coarse finite element models. The present work removes these limitations, at least for Drucker–Prager type criteria where efficient second-order cone programming solvers are available. Extension to the, for most geomaterials, more accurate Mohr–Coulomb criterion can be achieved in an analogous manner by using the closely related methodology of semidefinite programming [18].

Finally, we note that the basic approach of replacing the original yield function with an approximate function that coincides with the plastic potential at the current stress point is generally applicable, both to perfectly plastic and to hardening models. Indeed, the methodology has recently been applied successfully to the modified Cam clay model [48, 49].

APPENDIX A: SECOND-ORDER CONE PROGRAMMING STANDARD FORM OF ELASTOPLASTICITY

Second-order cone programming makes use of the following standard form:

$$\begin{aligned} & \text{minimize} && \mathbf{c}^\top \mathbf{x} \\ & \text{subject to} && \mathbf{A} \mathbf{x} = \mathbf{b} \\ & && \mathbf{x}_i \in \mathcal{K}_i, \quad i = 1, \dots, n \end{aligned} \quad (\text{A.1})$$

where the solution vector, \mathbf{x} , is partitioned into n subvectors \mathbf{x}_i such that $\mathbf{x} = (\mathbf{x}_1, \dots, \mathbf{x}_n)^\top$. The cones may be either standard quadratic cones

$$\mathcal{K}_q : z_1 \geq \sqrt{\sum_{j=2}^{m+1} z_j^2} \quad (\text{A.2})$$

or rotated quadratic cones

$$\mathcal{K}_r : 2z_1 z_2 \geq \sum_{j=3}^{m+2} z_j^2, \quad z_1, z_2 \geq 0 \quad (\text{A.3})$$

The problem of step-by-step elastoplasticity can be cast in terms of a mathematical program as

$$\begin{aligned} & \text{maximize} && -\frac{1}{2}(\boldsymbol{\sigma} - \boldsymbol{\sigma}_0)^\top \mathbf{C}^e (\boldsymbol{\sigma} - \boldsymbol{\sigma}_0) \\ & \text{subject to} && \mathbf{B}^\top \boldsymbol{\sigma}_j = \mathbf{p} \\ & && F_j(\boldsymbol{\sigma}_j) \leq 0, \quad j = 1, \dots, n_\sigma \end{aligned} \quad (\text{A.4})$$

where $\boldsymbol{\sigma}$ is the unknown stress state (previously denoted $\hat{\boldsymbol{\sigma}}_{n+1}$) and $\boldsymbol{\sigma}_0$ is the known stress state (previously denoted $\hat{\boldsymbol{\sigma}}_n$). It has here been assumed that the stress vector $\boldsymbol{\sigma}$ is partitioned into n_σ subvectors such that $\boldsymbol{\sigma} = (\boldsymbol{\sigma}_1, \dots, \boldsymbol{\sigma}_{n_\sigma})^\top$ and that a separate yield condition $F_j \leq 0$ is enforced for each of these subvectors. In standard finite element formulations, this would correspond to enforcing the yield condition at each Gauss point.

Furthermore, in standard finite element formulations, the elastic compliance matrix, \mathbf{C}^e , is block-diagonal, so that we have

$$\frac{1}{2}(\boldsymbol{\sigma} - \boldsymbol{\sigma}_0)^\top \mathbf{C}^e (\boldsymbol{\sigma}_0 - \boldsymbol{\sigma}_0) = \sum_{j=1}^{n_\sigma} \frac{1}{2}(\boldsymbol{\sigma}_j - \boldsymbol{\sigma}_{j,0})^\top \mathbf{C}_j (\boldsymbol{\sigma}_j - \boldsymbol{\sigma}_{j,0}) \quad (\text{A.5})$$

The original mathematical programming problem (A.4) can then be written as

$$\begin{aligned} & \text{minimize} && \sum_{j=1}^{n_\sigma} \frac{1}{2}(\boldsymbol{\sigma}_j - \boldsymbol{\sigma}_{j,0})^\top \mathbf{C}_j^e (\boldsymbol{\sigma}_j - \boldsymbol{\sigma}_{j,0}) \\ & \text{subject to} && \mathbf{B}^\top \boldsymbol{\sigma} = \mathbf{p} \\ & && F_j(\boldsymbol{\sigma}_j) \leq 0, \quad j = 1, \dots, n_\sigma \end{aligned} \quad (\text{A.6})$$

or equivalently as

$$\begin{aligned} & \text{minimize} && \sum_{j=1}^{n_\sigma} t_j \\ & \text{subject to} && \mathbf{B}^\top \boldsymbol{\sigma} = \mathbf{p} \\ & && F_j(\boldsymbol{\sigma}_j) \leq 0, \quad j = 1, \dots, n_\sigma \\ & && 2s_j t_j \geq (\boldsymbol{\sigma}_j - \boldsymbol{\sigma}_{j,0})^\top \mathbf{C}_j^e (\boldsymbol{\sigma}_j - \boldsymbol{\sigma}_{j,0}), \quad j = 1, \dots, n_\sigma \\ & && s_j = 1, j = 1, \dots, n_\sigma \end{aligned} \quad (\text{A.7})$$

where s_j and t_j are auxiliary variables. The original quadratic objective function here has been substituted for a linear objective function and a set of inequalities (which ultimately will be satisfied with equality). Provided that F_j are of the Drucker–Prager type, it is straightforward to introduce new variables to bring these yield constraints on quadratic conic form. Similarly, the inequalities stemming from the quadratic objective function can be cast in terms of n_σ rotated quadratic cones so that the final problem complies with the standard form (A.1).

REFERENCES

1. Rice JR. The localization of plastic deformation. In *Theoretical and Applied Mechanics*, Koiter W (ed.). North-Holland: Amsterdam, 1976; 239–264.
2. Leroy Y, Ortiz M. Finite element analysis of strain localization in frictional materials. *International Journal for Numerical and Analytical Methods in Geomechanics* 1989; **13**:53–74.
3. Bigoni D, Hueckel T. Uniqueness and localization—I. Associative and non-associative elastoplasticity. *International Journal of Solids and Structures* 1991; **2**:197–213.
4. Runesson K, Ottosen NS, Peric D. Discontinuous bifurcations of elastic–plastic solutions at plane stress and plane strain. *International Journal of Plasticity* 1992; **7**:99–121.
5. Borja RI. Conditions for instabilities in collapsible solids including volume implosion and compaction banding. *Acta Geotechnica* 2006; **1**:107–122.
6. Andrade JE, Borja RI. Capturing strain localization in dense sands with random density. *International Journal for Numerical Methods in Engineering* 2006; **67**:1532–1564.
7. Manzari MT, Nour MA. Significance of soil dilatancy in slope stability analysis. *Journal of Geotechnical and Geoenvironmental Engineering* 2000; **126**:75–80.
8. Carter JP, Poon MSB, Airey DW. Numerical and semi-analytical techniques for footings subjected to combined loading. *Proc IACMAG 11*, Turin, 2005; 163–176.
9. Clausen J, Krabbenhoft K. Existence and uniqueness of solutions in nonassociated Mohr–Coulomb elastoplasticity. *Proc. WCCM VIII*, Venice, 2008.
10. Loukidis D, Salgado R. Bearing capacity of strip and circular footings in sand using finite elements. *Computers and Geotechnics* 2009; **36**:871–879.
11. Simo JC, Taylor RL. Consistent tangent operators for rate-independent elastoplasticity. *Computer Methods in Applied Mechanics and Engineering* 1985; **48**:101–118.

12. Simo JC, Hughes TJR. *Computational Inelasticity*. Springer-Verlag: New York, 1998.
13. Krabbenhoft K, Lyamin AV, Sloan SW, Wriggers P. An interior-point method for elastoplasticity. *International Journal for Numerical Methods in Engineering* 2007; **69**:592–626.
14. Krabbenhoft K, Lyamin AV, Sloan SW. Formulation and solution of some plasticity problems as conic programs. *International Journal of Solids and Structures* 2007; **44**:1533–1549.
15. Krabbenhoft K. A variational principle of elastoplasticity and its application to the modeling of frictional materials. *International Journal of Solids and Structures* 2009; **46**:464–479.
16. Krabbenhoft K, Lyamin AV, Sloan SW. Associated plasticity for nonassociated frictional materials. *Proc. NUMGE*, Trondheim, Norway, 2010.
17. Souza de Neto EA, Peric D, Owen DJR. *Computational Methods for Plasticity: Theory and Applications*. Elsevier: Amsterdam, 2009.
18. Krabbenhoft K, Lyamin AV, Sloan SW. Three-dimensional Mohr–Coulomb limit analysis using semidefinite programming. *Communications in Numerical Methods in Engineering* 2008; **24**:1107–1119.
19. Bowden FP, Tabor D. *Friction. An Introduction to Tribology*. Anchor Press/Doubleday: New York, 1973.
20. Genna F, Pandolfi A. Accurate numerical integration of Drucker–Prager’s constitutive equations. *Meccanica* 1994; **29**:239–260.
21. Hjjaj M, Fortin J, de Saxce G. A complete stress update algorithm for the non-associated Drucker–Prager model including treatment of the apex. *International Journal of Engineering Science* 2003; **41**:1109–1143.
22. Krabbenhoft K, Lyamin AV, Hjjaj M, Sloan SW. A new discontinuous upper bound limit analysis formulation. *International Journal for Numerical Methods in Engineering* 2005; **63**:1069–1088.
23. Koiter WT. Stress–strain relations, uniqueness and variational theorems for elastic–plastic materials with a singular yield surface. *Quarterly of Applied Mathematics* 1953; **11**:350–354.
24. Fletcher R. *Practical Methods of Optimization*. John Wiley & Sons, Inc.: New York, 1987.
25. Lyamin AV, Sloan SW. Lower bound limit analysis using non-linear programming. *International Journal for Numerical Methods in Engineering* 2002; **55**:573–611.
26. Lyamin AV, Sloan SW. Upper bound limit analysis using linear finite elements and non-linear programming. *International Journal for Numerical and Analytical Methods in Geomechanics* 2002; **26**:181–216.
27. Krabbenhoft K, Damkilde L. A general nonlinear optimization algorithm for lower bound limit analysis. *International Journal for Numerical Methods in Engineering* 2003; **56**:165–184.
28. Lyamin A, Krabbenhoft K, Abbo A, Sloan S. General approach to modelling discontinuities in limit analysis. In *Proceedings of IACMAG*, Turin, Barla G, Barla M (eds), 2005.
29. Lyamin AV, Sloan SW, Krabbenhoft K, Hjjaj M. Lower bound limit analysis with adaptive remeshing. *International Journal for Numerical Methods in Engineering* 2005; **63**:1961–1974.
30. Lyamin AV, Krabbenhoft K, Sloan SW, Hjjaj M. An adaptive algorithm for upper bound limit analysis using discontinuous velocity fields. In *Proc. ECCOMAS 2004*, 2004; 1–11.
31. Weinstock R. *Calculus of Variations with Applications to Physics and Engineering*. Dover: New York, 1974.
32. Zouain N, Herskovits J, Borges LA, Feijóo RA. An iterative algorithm for limit analysis with nonlinear yield functions. *International Journal of Solids and Structures* 1993; **30**(10):1397–1417.
33. Borges LA, Zouain N, Huespe AE. A nonlinear optimization procedure for limit analysis. *European Journal of Mechanics, A/Solids* 1996; **15**(3):487–512.
34. Andersen ED, Roos C, Terlaky T. On implementing a primal–dual interior-point method for conic quadratic optimization. *Mathematical Programming* 2003; **95**:249–277.
35. Ben-Tal A, Nemirovski A. *Lectures on Modern Convex Optimization: Analysis, Algorithms, and Engineering Applications*, MPS-SIAM Series on Optimization. SIAM: Philadelphia, 2001.
36. Frydman S, Burd HJ. Numerical studies of bearing-capacity factor n_γ . *Journal of Geotechnical and Geoenvironmental Engineering* 1997; **123**:20–29.
37. Yin JH, Wang YJ, Selvadurai APS. Influence of nonassociativity on the bearing capacity of a strip footing. *Journal of Geotechnical and Geoenvironmental Engineering* 2001; **127**:985–989.
38. Erickson HL, Drescher A. Bearing capacity of circular footings. *Journal of Geotechnical and Geoenvironmental Engineering* 2002; **128**:38–43.
39. Mabrouki A, Benmeddour D, Frank R, Mellas M. Numerical study of the bearing capacity for two interfering strip footings on sands. *Computers and Geotechnics* 2010; **37**:431–439.
40. Drescher A, Detournay E. Limit load in translational failure mechanisms for associative and non-associative materials. *Geotechnique* 1993; **43**(3):443–456.
41. Davis EH. Theories of plasticity and the failure of soil masses. In *Soil Mechanics: Selected Topics*, Lee IK (ed.). Butterworth: London, 1968; 341–380.
42. Nordal S. Can we trust numerical collapse load simulations using nonassociated flow rules? *Proc. 12th Int. Conf. IACMAG*, Goa, India, 2008.
43. Gajo A, Bigoni D, Wood DM. Multiple shear band development and related instabilities in granular materials. *Journal of the Mechanics and Physics of Solids* 2004; **52**:2683–2724.
44. Chen WF, Liu XL. *Limit Analysis in Soil Mechanics*. Elsevier Science Publishers B.V.: Amsterdam, 1990.
45. Hjjaj M, Lyamin AV, Sloan SW. Numerical limit analysis solutions for the bearing capacity factor N_γ . *International Journal of Solids and Structures* 2005; **42**:1681–1704.

46. Sloan SW, Kleeman PW. Upper bound limit analysis using discontinuous velocity fields. *Computer Methods in Applied Mechanics and Engineering* 1995; **127**:293–314.
47. Merifield RS, Sloan SW. The ultimate pullout capacity of anchors in frictional soils. *Canadian Geotechnical Journal* 2006; **43**:852–868.
48. Krabbenhoft K, Lyamin AV, Sloan SW, Vicente da Silva M. Mathematical programming formulation of elasto-plastodynamics for geomaterials. In *Proc. 2nd Int. Symp. Comp. Geomech. (ComGeo II)*, Pietruszczak S, Pande GN (eds). International Center for Computational Engineering, 2011.
49. Krabbenhoft K, Lyamin AV. Computational Cam clay plasticity using second-order cone programming. *Computer Methods in Applied Mechanics and Engineering* 2011. In press.